Icarus 449 (2026) 116967

Contents lists available at ScienceDirect

Icarus

journal homepage: www.elsevier.com/locate/icarus

Research Paper

Radiatively coupled equatorial waves in Mars' Aphelion Cloud Belt: Wavenumber–frequency analysis in Mars GCM simulations

Márton Mester [a,*], R. John Wilson [b], Melinda A. Kahre [b]

[a] NASA Postdoctoral Program, NASA Ames Research Center, Moffett Field, 94035, CA, United States of America
[b] Space Science and Astrobiology Division, NASA Ames Research Center, Moffett Field, 94035, CA, United States of America

ARTICLE INFO

Dataset link: Radiatively Coupled Equatorial Waves in Mars' Aphelion Cloud Belt: Wavenumber--Frequency Analysis in Mars GCM Simulations (Original data)

Keywords:
Mars, atmosphere
Mars, climate
Atmospheres, dynamics

ABSTRACT

We investigate the influence of radiatively active water–ice clouds on tropical wave variability in Mars' Aphelion Cloud Belt using Mars general circulation model simulations. Wavenumber–frequency spectral and empirical orthogonal function analyses reveal four primary categories of variability: fast eastward- and westward-propagating waves, slow eastward and westward oscillations associated with the Tropical Cloud Oscillation (TCO), and the diurnal westward-propagating wavenumber-1 tide (DW1). When water–ice clouds are radiatively active, the spectrum of tropical variability is dominated by a 13-sol, eastward-propagating wavenumber-1 mode and a 7-sol, westward-propagating wavenumber-2 mode. Both exhibit vertically coherent, quasi-barotropic structures in the cloud field but distinct baroclinic signatures in temperature, indicating partial dynamical coupling between thermal and microphysical variability. By contrast, simulations without radiatively active clouds display more distinct Kelvin and Rossby wave-like bands and qualitatively different spatial structures among slow waves. Radiative feedbacks redistribute energy and concentrate the spectral distribution to a discrete set of wave modes, and promote vertically extended, hemispherically coupled wave modes. The slow TCO-related variability is particularly sensitive to cloud radiative effects. With radiatively active clouds, the long-period spectral wave band forms a robust three-state oscillation involving alternating cloudiness over Tharsis and Syrtis Major — consistent with observations. However, in the absence of radiative feedbacks, the variability collapses into a single, slowly propagating mode confined to Tharsis. These results demonstrate that radiatively active water–ice clouds fundamentally reshape the spectrum and structure of Martian tropical waves. By introducing vertically distributed diabatic heating and enhancing thermal–microphysical coupling, cloud radiative effects sustain the large-scale, seasonally modulated oscillations that characterize the tropical cloud regime on Mars.

1. Introduction

The Aphelion Cloud Belt (ACB) of Mars is a seasonally recurring tropical cloud structure that encircles the planet at low latitudes (Clancy et al., 1996). It develops during the post vernal equinox season ($L_s = 0–70°$, where L_s denotes solar longitude and $L_s = 0°$ corresponds to northern vernal equinox), intensifies after aphelion ($L_s = 71–135°$, Wolff et al., 2019; Guha et al., 2021b) and weakens in the period preceding autumnal equinox ($L_s = 135–180°$). The ACB's spatial structure and temporal evolution have been analyzed primarily from data provided by instruments on the sun-synchronous polar orbiters Mars Global Surveyor (MGS) and Mars Reconnaissance Orbiter (MRO). MGS' instruments retrieved data at 2 am and 2 pm local times each day between 1997–2006, and MRO's instruments have been retrieving data at 3 am and 3 pm local time since 2006. The twice-daily retrievals of MGS and MRO and recent retrievals from the Emirates Mars Mission (EMM), which occupies a highly elliptical orbit around Mars and provides a more complete local time coverage, have uncovered qualitative differences between daytime clouds and nighttime clouds in altitudinal and zonal structure (Wolff et al., 2019, 2022). During daytime, clouds may occupy a wide range of heights between a few kilometers to several tens of kilometers above ground level, and this structure is accompanied with a near-surface cloud blanket that develops during nighttime (Wilson et al., 2007). Topographic influences are understood to modulate the formation and distribution of the ACB (Wang and Ingersoll, 2002; Guha et al., 2021a; Fernando et al., 2023). Elevated terrain, such as the Tharsis volcanic plateau, Syrtis Major, Elysium Mons, and the Arabia Terra highlands, induces orographic lifting of moist air masses, enhancing local condensation and water–ice cloud formation. Furthermore, Tharsis and Arabia Terra/Syrtis Major are

* Corresponding author.
E-mail addresses: marton.mester@nasa.gov (M. Mester), robert.j.wilson@nasa.gov (R.J. Wilson), melinda.a.kahre@nasa.gov (M.A. Kahre).

https://doi.org/10.1016/j.icarus.2026.116967
Received 26 November 2025; Received in revised form 13 January 2026; Accepted 21 January 2026
Available online 22 January 2026
0019-1035/© 2026 Elsevier Inc. All rights are reserved, including those for text and data mining, AI training, and similar technologies.

associated with low thermal inertia, which helps promote nighttime cloud formation. These orographic and thermal effects lead to spatial heterogeneity within the otherwise latitudinally confined cloud belt, with persistent cloud formation over elevated volcanic regions and adjacent slopes. These influences, and a subsolar point that is located at the northern hemisphere during the aphelion season, result in an ACB that is characterized by a spatial structure that is not symmetric about the equator, but is shifted to occupy the 15°S–30°N latitude band (Wang and Ingersoll, 2002; Guha et al., 2021b; Sánchez-Lavega et al., 2025).

The radiative influence of ACB clouds is a key component of the Martian climate system. Unlike Earth, where latent heat and convection dominate, Mars' cloud–climate interactions are primarily radiative in nature (Richardson et al., 2002; Steele et al., 2014; Wilson and Guzewich, 2014). The radiative effects have a dual role: the absorption of longwave (IR) radiation from the hot daytime surface warms the cloud layer; however, the reflection of incoming solar (shortwave) radiation increases albedo and decreases insolation at the surface. At night, water–ice clouds act as efficient radiators in the infrared, resulting in radiative cooling at cloud tops and enhanced downward IR radiation to the surface (Hinson and Wilson, 2004; Wilson et al., 2007; Wilson and Guzewich, 2014). The net result is a reduction in the diurnal range of surface temperature and an increase in atmospheric temperature (Wilson et al., 2008; Madeleine et al., 2012; Kahre et al., 2015). Furthermore, the combination of daytime atmospheric heating and nighttime cooling leads to enhanced forcing of the semidiurnal temperature tide (Wilson et al., 2014; Haberle et al., 2019).

A recently identified component of the ACB's intra-seasonal variability is the Tropical Cloud Oscillation (TCO) (Wang and González Abad, 2021), characterized by slow oscillations in cloud intensity between the 'eastern' and 'western' hemispheres, centered on the continental-scale highlands Tharsis and Syrtis Major. The TCO has been interpreted as slow, 10–40 sol period (sol = 1 Martian day) oscillations of the ACB. The first wavenumber–frequency analysis of these slow cloud oscillations was recently performed by Wang et al. (2024, W24 hereafter). They used blue-filtered Mars Daily Global Maps (MDGMs) (Wang et al., 2020), processed from MRO Mars Color Imager (MARCI) imagery, to track the evolution of the cloud field in 7 Mars Years (MYs) at each 0.5° latitude bin within the 20°S–20°N latitude band. A mean spectrum was obtained by averaging spectra from all segments. Instead of the more common practice in terrestrial equatorial wave dynamics, which determines and removes a background spectrum via 1-2-1 filtering, W24 determined the standard deviation σ of the power at each wavenumber–frequency by considering all 96-sol-length segments. Then, on the individual spectra of any segment, 'active' waves were determined by applying either a 1-σ or 2-σ threshold, and attention was restricted to such waves. W24 motivated the use of this alternative technique by noting that the MRO spacecraft's observation pattern and the substantial local-time variation of tropical clouds resulted in spurious peaks throughout the analyzed data record, rendering the data difficult to interpret. Nonetheless, W24 found that 'active' waves with the highest power are typically (with some segment-to-segment variability) a westward-propagating wavenumber-1 wave with 33–50 sol period and two eastward-propagating wavenumber-1 waves, one with 12.5 sol period and one with 20–33 sol. While this method may be applicable for extracting key wave modes from imagery and might be a beneficial approach given the limitations in observations, it does not reveal the relevant wave bands (e.g., Kelvin waves or equatorial Rossby waves).

To further elucidate their results, W24 superposed idealized equatorial β-plane dispersion curves with various equivalent depths on the wavenumber–frequency spectra. It claimed that the key modes are Kelvin and equatorial Rossby waves. However, the wavenumber–frequency spectra did not demonstrate this as clearly as it does in terrestrial equatorial wave studies. Perhaps the typical approach of background spectrum removal (using data from another ongoing or future mission) could isolate the Kelvin and equatorial Rossby wave bands more clearly. Nonetheless, the determined long-period wavenumber-1 structures provide a valuable starting point in understanding TCO dynamics.

In the present study, we perform Mars Global Climate Model (MGCM) experiments to further analyze oscillations in tropical clouds and cloud-level temperatures during L_s = 0–180°. The main objectives of this work are the characterization of significant wave bands comprising fast and moderate waves with 1–20 sol periods, and slow waves with periods longer than 20 sols that drive the TCO, as well as assessment of the influence of cloud–climate radiative feedbacks on the most significant wave modes. Our baseline experiment, incorporating water–ice cloud microphysics and an annually repeating dust scenario, is used to compute wavenumber–frequency spectra of tropical cloud and temperature variability during L_s = 0–180°. We determine and remove a background spectrum to robustly isolate statistically significant wave bands and modes. The horizontal and vertical structures of the most significant modes among the fast-to-moderate and slow waves are presented and interpretations of potential Kelvin- or Rossby-wave-like patterns are explored and discussed. An empirical orthogonal function (EOF) analysis is also performed further to elucidate the spatio-temporal variability within each significant wave band. Since radiative effects dominate cloud–climate interactions on Mars rather than convection, certain wave bands may be amplified or suppressed by radiative feedbacks. We explore the extent of radiative feedbacks on the significant wave bands, including fast-moderate and slow waves, by performing an additional experiment, in which we turn off the radiative properties of the water–ice clouds completely.

The paper is structured as follows. Section 2 describes the model and methodology. Section 3 presents our results, Section 4 provides a discussion, and Section 5 summarizes the conclusions.

2. Methods

2.1. The NASA Ames Mars Global Climate model

The NASA Ames MGCM version 3.2 employs a cubed-sphere grid and finite-volume dynamical core developed by NOAA/GFDL (Harris et al., 2021), coupled with physics schemes from the NASA Ames Legacy Mars GCM (Haberle et al., 2019). Surface properties are represented using albedo maps derived from MGS Mars Orbiter Laser Altimeter (MOLA) data (Putzig and Mellon, 2007), and thermal inertia data based on Viking and Thermal Emission Spectrometer (TES) observations (Tyler and Barnes, 2014). For our simulations, the MGCM was run at a horizontal resolution of 'c48', meaning each face of the cubesphere grid is divided into a 48 × 48 subgrid. The vertical structure uses a hybrid sigma-pressure coordinate system (Simmons and Burridge, 1981) with 56 layers, providing a resolution ~5 m near the surface and about 5 km near the model top (80–90 km altitude). Model output is interpolated horizontally to a 2° × 2° longitude–latitude grid and vertically to a standard pressure grid during post-processing.

2.1.1. Water–ice microphysics scheme

The model includes the water–ice microphysics package, as detailed in Haberle et al. (2019). This package explicitly simulates the microphysical processes involved in the formation and evolution of water–ice clouds in the Martian atmosphere (Kahre et al., 2024). This includes heterogeneous ice nucleation on airborne dust particles, as well as growth by condensation, sedimentation, and sublimation. The scheme treats the dust as cloud condensation nuclei, allowing for calculation of cloud particle number and mass mixing ratios, which are advected and diffused alongside other tracers in the model. Radiative interactions between water–ice clouds and solar/thermal infrared radiation may be optionally included, resulting in radiatively active or inert clouds. The radiatively active option enables the representation of cloud–radiative

Table 1
Summary of experiment configurations.

Experiment id	Cloud-radiation settings	Dust scenario	Simulation length	Resolution
RAC	Radiatively active clouds	MY 30	10 MYs, first 5 MYs discarded	c48 (2° × 2°)
noRAC	Radiatively inert clouds	MY 30	10 MYs, first 5 MYs discarded	c48 (2° × 2°)

feedbacks that influence atmospheric dynamics and the distribution of water vapor.

We track the evolution of the clouds through two variables: the moment-based variable μ, a tracer that represents water–ice cloud particle mass mixing ratio (output variable *ice_mass_mom*), and the column-integrated visible optical depth τ due to water–ice clouds (output variable *taucloud_VIS*), that the model determines only when the radiative option is switched on.

2.1.2. Dust forcing

While the GCM supports multiple dust column representations (see e.g., Bertrand et al. (2020)), we adopt a simple, prescribed dust scenario designed to replicate Mars Year (MY) 30 conditions for all simulated years. This approach imposes an annually repeating column-integrated dust distribution, effectively minimizing interannual variability in dust loading and its impact on tropical wave activity. The advantage of using a single-year dust scenario is that it allows for a more consistent identification of dominant wave modes, reducing ambiguity introduced by year-to-year variability. However, this choice also limits the model's ability to capture wave structures that may emerge under different dust conditions, particularly those suppressed during the relatively quiescent MY 30. The reader should be aware of this limitation. We use the MY 30 dust scenario as it provides a representative seasonal variation of dust column opacity through the L_s = 0–180° period (Montabone et al., 2015). The vertical distribution of dust is determined through both by microphysical interactions with the water–ice clouds and transport; dust is injected at the lowest model layer to match the prescribed horizontal dust opacity. The airborne dust is then transported by model winds or sedimented by gravity.

2.2. Model experiments

We execute two MGCM experiments to analyze the oscillatory cycles in the simulated Aphelion Cloud Belt. Our baseline simulation, denoted by **RAC**, includes radiatively active water–ice clouds. We begin our analysis by characterizing the dominant wave bands in this configuration. Next, we isolate the impact of cloud radiative feedbacks by conducting a further experiment, **noRAC**, where water–ice clouds are permitted to form but are radiatively inert - their interactions with solar and infrared radiation are disabled.

Each simulation spans 10 MYs, with the first 5 MYs discarded to allow for spin-up of the water cycle. We note that while Earth GCMs may require longer time to reach equilibrium, Mars GCMs in general do not need long spin-up periods as Mars' atmosphere and surface materials have low density and heat capacity, resulting in much lower thermal inertia than what is characteristic to Earth. Notably, previous studies have shown that a 5-MY spin-up time is sufficient for the Martian water cycle to reach an annually repeating state (Haberle et al., 2019). A summary on the experiment configurations are presented in Table 1.

2.3. Wavenumber–frequency analysis

Our analysis of the wavenumber–frequency spectrum follows standard procedures widely used in Earth's tropical wave studies (Wheeler and Kiladis, 1999; Frank and Roundy, 2006). Spectral quantities are computed from 5 MYs of model output in the L_s = 0–180° season, each lasting 372 sols (Martian days, one sol = 24.66 Earth hours). The reader should be aware that we will continue to refer to 'sols' rather than 'days' in the paper. Correspondingly, the nomenclature of 'cycles per day, (cpd)' commonly used in Earth atmosphere investigations will be replaced by 'cycles per sol, (cps)', clarifying that wave periods are to be calculated in Martian days rather than Earth days. We employ Welch's method (Welch, 1967) to estimate the wavenumber–frequency spectrum. Each seasonal time series is divided into seven overlapping segments, with each segment overlapping the next by 50%, resulting in 93-sol segments. Within each segment, the linear trend is removed, and a Hamming window is applied to reduce spectral leakage. A complex two-dimensional Fast Fourier Transform (FFT) is then performed on each segment, and the power spectral density (PSD) is calculated as the squared magnitude of the FFT. The PSD is normalized by the number of segments to yield the average power, and further corrected by the sum of squared window values to account for power loss due to tapering. This procedure is applied at each latitude between 15°S and 30°N, and the resulting spectral power is averaged across all latitudes (between 15°S and 30°N) and years. To isolate significant spectral features, we determine and remove a background spectrum using a 1-2-1 smoothing filter repeatedly applied in both frequency and wavenumber dimensions. The effective spectral resolution is 1/93 cycles per sol (cps) and 1 unit wavenumber. Since the Aphelion Cloud Belt is not equatorially centered, we do not perform a symmetric–antisymmetric decomposition of the wave fields in this study.

In this work, we analyze the wavenumber–frequency spectrum of selected variables related to cloud structure and temperature. To determine a vertical level that is relevant to our investigations, we calculate the height–longitude structure of the seasonal mean of μ in the ACB in experiment **RAC** (Fig. 1(a)) and the seasonal evolution of the vertical structure of the zonally averaged temperature and water–ice mass mixing ratio (Fig. 1(b)). The bulk of the cloud belt is located between the 160–180 K isotherms (Fig. 1(b)), the latter being a rough approximation of the water–ice cloud condensation level which may vary depending on temperature and water mixing ratio. Based on the zonal structure of the clouds (Fig. 1(a)), pressure as a vertical coordinate looks to be a more relevant choice to study the horizontal propagation of waves in the ACB rather than above ground level height, since the seasonally averaged cloud bottom is located between 150–200 Pa at all longitudes and expresses little variations, apart from the source regions Syrtis Major (50°E) and Tharsis (250°E). The peak of water–ice cloud mass mixing ratio varies with longitude; however, the 70 Pa level seemingly corresponds to a region that is relevant to the cloud belt dynamics at each longitude (Fig. 1(a)) at any time (Fig. 1(b)). Furthermore, the 70 Pa pressure level is the highest value on our pressure grid, which is always located above the highest point of the surface (i.e., the point of lowest surface pressure, not shown), and therefore spatial wave decomposition is possible at all times.

This study aims to interpret the oscillations of the Aphelion Cloud Belt in MGCM simulations. Our key prognostic variable for the purpose of analyzing wavenumber–frequency spectra in the clouds is the column-integrated visible optical depth due to water–ice clouds (τ), and the vertical structure of the cloud waves is determined from water–ice mass mixing ratio (μ); our primary analysis will rely on these two variables. To compare cloud waves with temperature waves, we also consider water–ice cloud particle mass mixing ratio at 70 Pa (μ_{70}) and temperature at 70 Pa (T_{70}); the 70 Pa level is chosen as it is considered to be a height that represents the mean cloud structure reasonably well (see discussion above). While the 70 Pa level is expected to capture most of the variability of the cloud belt, the reader should be aware that such a choice may not capture cloud or temperature waves at other heights, including waves that are constrained to the cloud bottom or top. The comparison aims to provide more confidence in determining the relevant equatorial wave bands and to analyze the extent to which temperature and cloud waves are coupled.

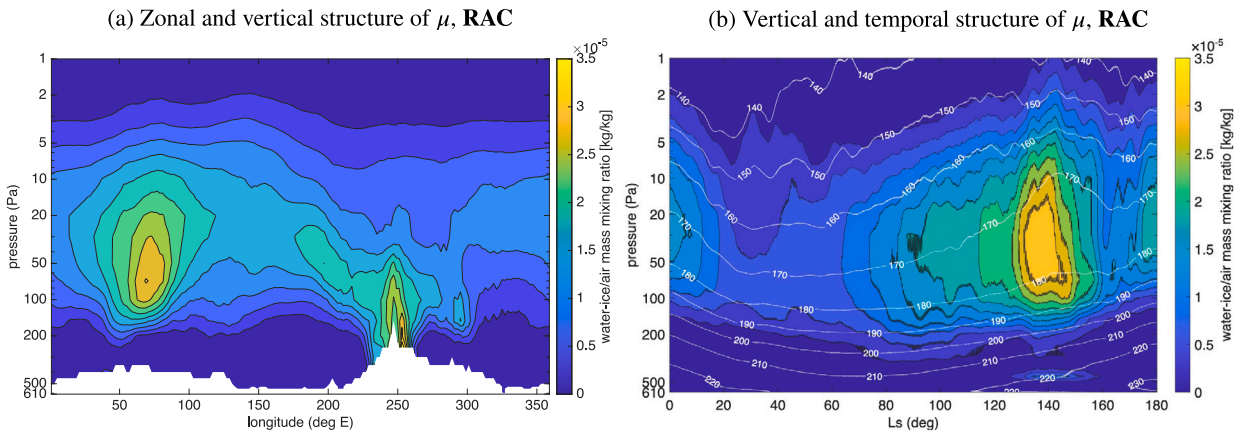


Fig. 1. (a) Five-year time mean of water–ice cloud mass mixing ratio, averaged over the $L_s = 0$–$180°$ period at 1°S, in experiment **RAC**. Topographic peaks located at 50°E (Syrtis Major) and 250° (Tharsis) are source regions of water–ice cloud formation. (b) Vertical and temporal structure of the climatological (i.e., 5-year mean) zonal mean of water–ice cloud mass mixing ratio (color contours) and temperature (white lines) at 1°S, in experiment **RAC**. (For interpretation of the references to color in this figure legend, the reader is referred to the web version of this article.)

2.4. Empirical orthogonal function analysis

To aid in the interpretation of the spatial and vertical structures of the dominant wave modes and specific spectral bands identified from the wavenumber–frequency analysis of τ, μ_{70} and T_{70}, we follow a standard empirical orthogonal function (EOF) analysis (for applications to equatorial waves on Earth, see e.g., Matthews, 2000; Wheeler and Hendon, 2004). The targeted wave mode or spectral band is first isolated by applying an inverse Fast Fourier Transform to the selected range of wavenumbers and frequencies. The covariance matrix is then computed over longitude and time, and its eigenvectors and eigenvalues represent the spatial patterns (EOFs) and their corresponding normalized variances (principal components), respectively. The EOFs are normalized so that the total of point-wise amplitude squared equals 1. When two EOFs account for the same fraction of variance and exhibit spatial patterns that are identical but phase-shifted by 90°, they may be interpreted as a quadrature pair representing a propagating wave mode.

The mode that corresponds to the oscillations of any (i.e., not necessarily a quadrature) pair $EOF1$ and $EOF2$ can be formulated as

$$\iota(\lambda,\theta,t) = PC1(t) \times EOF1(\lambda,\theta) + PC2(t) \times EOF2(\lambda,\theta), \quad (1)$$

where λ is longitude, θ is latitude, and PCk is the principal component time series corresponding to $EOFk$. The amplitude and phase of the combined mode ι are given by the amplitude and phase of the complex quantity $PC1(t) + iPC2(t)$ (see e.g., Matthews, 2000).

3. Wavenumber–frequency analysis

First, we consider experiment **RAC** to determine the wavenumber–frequency spectra of the variables τ, μ_{70} and T_{70}. The obtained background spectrum, and the wavenumber–frequency spectrum after the removal of the background spectrum, are presented on Fig. 2(a–d) for the column-integrated visible optical depth due to water–ice clouds (τ) and 70 Pa temperature (T_{70}).

3.1. Tropical waves in experiment *RAC*

3.1.1. Background spectrum

The background spectrum has a 'red' component, characterized by high energy density as cps approaches zero. This component exhibits high energy density at all wavenumbers for integer values of cps. The result that the wave spectrum has strong energy density at integer values of cps is not surprising, as thermal tides are especially prominent components of the Martian circulation. As shown on Fig. 2(a), the energy density at cps = 0 is higher than, but comparable with cps = 1 for τ, suggesting that the diurnal (i.e., 1-sol period) variability is similar, but weaker than the long-period oscillations in the cloud belt. The background spectra for each variable, μ_{70} and T_{70}, are found to be similar (not shown) and well described by an energy-density pattern with a red component and high-energy strips about the tidal modes. The differences in the power of long-period and diurnal waves imply that for the cloud field, seasonal variations are stronger than daily variations. In contrast, diurnal tides dominate seasonal variations in temperature.

3.1.2. Wavenumber–frequency spectrum comparison and wave band definitions

To analyze the tropical wave spectrum, the background spectrum is removed in order to isolate dynamically coherent variability associated with organized, large-scale modes, rather than the broadband variance produced by weakly or non-organized disturbances. Without this step, the signal of interest is masked by a nearly isotropic background that dominates the raw spectrum. The weak dependence of the background spectrum on zonal wavenumber in Fig. 2(a) reflects the fact that it is dominated by stochastic, short-lived fluctuations whose spatial scales are set primarily by local processes rather than by global wave geometry. As a result, this background variance is approximately uniform across zonal wavenumber, in contrast to the distinct wavenumber-dependent peaks associated with organized variability. Subtracting the background therefore does not impose a structure on the spectrum, but instead removes variance that lacks clear dynamical organization, allowing the physically meaningful spectral features to be identified more clearly.

The resulting wave spectra for τ, μ_{70} and T_{70} show remarkable similarities and differences (Fig. 2). First, the 70 Pa water–ice mass mixing ratio (μ_{70}) captures the key modes of variability in the column integrated opacity due to water–ice clouds (τ), both wave spectra are characterized by the presence of slow waves, both eastward and westward, with eastward wavenumber-1, -2 dominating. Furthermore, a westward wavenumber-2 is prominent with a period of approximately seven sols. A further prominent mode in τ is an eastward wavenumber-1 with a period of 13 sols. This wave is strong in μ_{70}, but not as dominant as in the column-integrated opacity. The moderate wave density at 0.3 cps across various wavenumbers is also present in both wave spectra, and the diurnal (i.e., 1-sol period) tides are clearly represented. Overall, the comparison suggests that the 70 Pa water–ice mass mixing ratio captures the relevant modes of the cloud belt oscillations. Therefore, it is meaningful to compare the spatial structure of the 70 Pa temperature modes with either μ_{70} or τ modes to analyze the extent to

which the cloud field is coupled to temperature. The wave spectrum of T_{70} similarly includes long-period waves; however, the mode with the highest power is the zonal wavenumber-1 mode rather than the wavenumber-2. High power westward waves occupy a similar region (wavenumbers 1–4 with cps 0.05–0.25); however, the 7–8-sol-period westward waves are dominated by wavenumber-1 components in T_{70}, as opposed to the wavenumber-2 dominances that are not present in the cloud field. Therefore, while the distributions of the high-power temperature and cloud modes on the spectrum express similarities, they also exhibit significant differences. Based on the similarities and differences of the wave spectra of the three key variables presented on Fig. 2(b–d), we distinguish several significant wave bands. A wave band K, speculated to be related to Kelvin waves based on its position on the wavenumber–frequency spectrum, is defined as long-medium eastward propagating waves (i.e., wavenumbers $k = 1-5$) of frequency $0.05 < \text{cps} < 0.7$. Furthermore, the band is constrained by the lines $\text{cps}/k = 0.03$ and $\text{cps}/k = 0.35$ that correspond to approximately 0.36 m and 50 m Kelvin wave equivalent depths, respectively. The K band clearly contains several strong temperature modes (Fig. 17(b)); however, the highest-power temperature modes do not clearly coincide with modes of high power in the cloud field. A possible exception is a wavenumber-1 wave with a period of approximately 13 sols, which will be considered in more detail. A separate wave band R, speculated to be linked to equatorial Rossby waves based on its position on the spectrum, is defined here as long-medium westward propagating waves (wavenumbers $k = -1$ to -5) with frequency $0.05 < \text{cps} < 0.25$. There is an agreement between temperature and clouds that there exist high-power westward wavenumber-1 and -2 waves with a 7-sol period. In each wavenumber–frequency spectrum (for variables τ, μ_{70}, and T_{70}), the R and K wave bands contain the most significant modes with periods longer than a sol, but less than 20 sols. To address slow waves, we define two additional wavebands, ME and MW, consisting of slow ($\text{cps} < 0.05$), eastward- and westward-propagating long-medium waves, respectively. We refer to these wave bands as M since the ME band is located at a similar position of the wavenumber–frequency spectrum as the Madden-Julian Oscillation (MJO) on Earth. However, even though it is not established what drives the slow waves on Mars, it is clear that ME waves are fundamentally different from the MJO as convection is weak in cloud–climate interactions on Mars. Finally, we will consider the structure of the most dominant tide mode (Wu et al., 2017), the diurnal westward propagating wavenumber-1 tide (commonly referred to as DW1).

3.1.3. K and R waves

The wavenumber–frequency spectrum derived from cloud opacity (τ) indicates that wave activity within the range $0.05 < \text{cps} < 1$ is dominated by an eastward-propagating wavenumber-1 mode with a period of approximately 13 sols, and a westward-propagating wavenumber-2 mode with a period of roughly seven sols. These modes belong to the K and R wave bands, respectively. To characterize the spatial structures associated with these dominant modes, the first two empirical orthogonal functions (EOFs) were computed for each wavenumber–frequency component. The leading EOFs are shown in Fig. 3. In both cases, the first and second EOFs form a quadrature pair representing propagating wave behavior and together account for approximately 95% of the total variance within each mode.

Interestingly, the two dominant waves exhibit opposite hemispheric amplitudes: the K wave is enhanced in the southern hemisphere, whereas the R wave attains greater amplitude in the northern hemisphere. Such hemispheric asymmetry in pure Kelvin and equatorial Rossby waves is not predicted by classical equatorial wave theory, suggesting a modulation by topographically or thermally induced spatial heterogeneity. The vertical structures in water–ice cloud mass mixing ratio associated with these two modes are calculated as a meridional mean through the tropics (15°S–30°N) and are shown in Fig. 4. The K mode exhibits its maximum amplitude near 20 Pa, remains prominent throughout the 2–70 Pa range, and displays a predominantly barotropic vertical structure. By contrast, the amplitude of the R mode remains nearly uniform between 5 and 70 Pa but exhibits an approximate 30° westward tilt over this pressure interval. The vertical structure of the K mode closely resembles that of dry equatorial waves obtained under a rigid-lid upper boundary condition (Haertel et al., 2008). In contrast, the R mode structure is more consistent with solutions employing a radiation upper boundary condition (Kiladis et al., 2009). Based on the cloud field alone, however, it remains challenging to assess the extent to which the observed K and R modes correspond to classical Kelvin and Rossby wave dynamics.

To further investigate the thermodynamic signature of the dominant modes, we examine their spatial patterns at 70 Pa (Fig. 5) and their vertical structures (Fig. 6) in temperature, rather than in water–ice mass mixing ratio. The analysis focuses on the ∼13-sol-period, eastward-propagating wavenumber-1 K wave and the ∼7-sol-period, westward-propagating wavenumber-2 R wave. The EOF analysis reveals that temperature variability at fixed wavenumber and period is less dominated by a single coherent spatial pattern than in the cloud field. For the K mode, the leading two EOFs — which form a quadrature pair and represent the propagating component — account for 87% of the total variance. By contrast, for the R mode, the first two EOFs together explain 66% of the variance. In contrast, the third and fourth EOFs contribute the remaining 34%, suggesting that the R mode comprises two distinct, overlapping wave components, denoted here by R_1 and R_2, respectively.

Curiously, neither the horizontal nor the vertical temperature structures closely resembles those derived from the cloud field. Unlike the southern-hemisphere-amplified K mode in τ, the temperature K wave is nearly symmetric about the equator between 15°S and 15°N, consistent with a Kelvin wave interpretation. The temperature R_1 wave, in contrast, exhibits strong hemispheric asymmetry, characterized by a sharp phase reversal near 10°S. Both the K and R_1 temperature modes show enhanced amplitudes north of 20°N, likely reflecting the influence of the midlatitude storm track.

The vertical structures of the temperature modes also differ qualitatively from those of the cloud-derived waves. Although the 13-sol, wavenumber-1 K wave is barotropic in μ, its temperature structure tilts eastward with height below 20–30 Pa and reverses to a westward tilt above this level. No clear feature in the vertical cloud structure appears to explain this qualitative transition in the temperature mode at 30 Pa. In addition, the temperature K mode exhibits a rapid phase shift near 3 Pa, coinciding approximately with the cloud top, where both the K and R_1 modes in cloud mass mixing ratio decay sharply (Fig. 6). The vertical structure of the R_1 mode is distinctly baroclinic, showing an eastward tilt with height — opposite to the westward tilt observed in the corresponding cloud R mode.

Overall, the temperature and cloud fields exhibit qualitative differences in both the K and R bands. Neither their horizontal nor vertical structures are consistent, and no clear dynamical coupling between the temperature and cloud wave modes can be identified.

3.1.4. ME waves

We start the analysis of slow waves by considering eastward and westward waves separately. The long-period eastward-propagating ME waves exhibit high power at wavenumbers 1–4, both in temperature and in cloud structure. The wave band does not indicate non-dispersive behavior, as the frequency of the highest-energy mode remains nearly constant across all wavenumbers. The presence of multiple wavenumbers and the dispersive behavior suggest that the leading mode of variability may not be a single-wavenumber wave. To further elucidate on this impression, we calculate the EOFs of the ME wave band in the cloud structure (i.e., in column-integrated visible optical depth due to water–ice clouds, τ). The first two EOFs form a pair; together explaining 68% of the variance of the ME band (34% each); the spatial structure of the two dominating EOFs is shown in Fig. 7. The

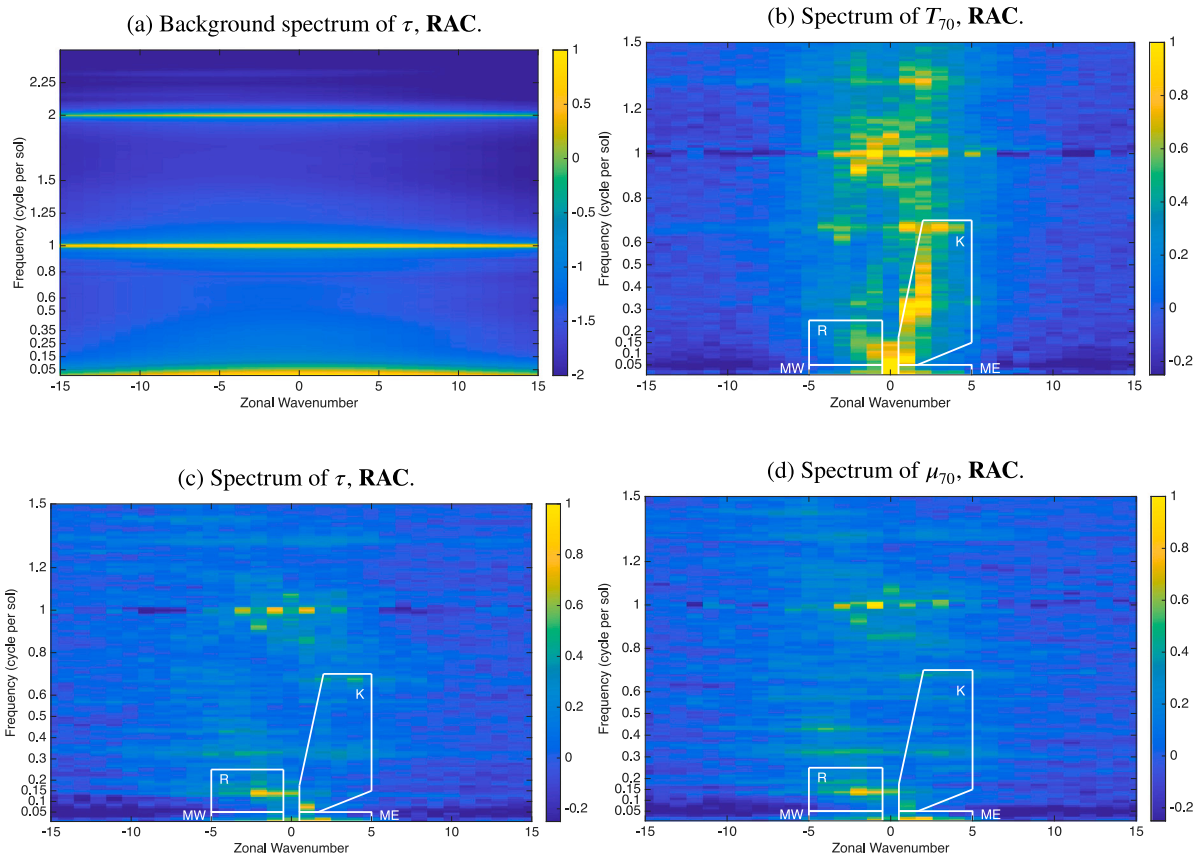


Fig. 2. Wavenumber–frequency spectra of water–ice cloud opacity τ (a, c) and 70 Pa temperature T_{70} (b) and 70 Pa water–ice mass mixing ratio μ_{70} (d) in experiment **RAC**. The background spectrum (shown only for τ) exhibits high power for long-period waves and tide harmonics (a). Upon removing the background spectrum, the significant wave bands are revealed (b, c, d). Solid white lines depict boundaries of wave bands K (long/medium eastward waves with periods longer than a sol, but less than 20 sols), R (long/medium westward waves with periods longer than a sol, but less than 20 sols), ME (slow eastward waves), and MW (slow westward waves).

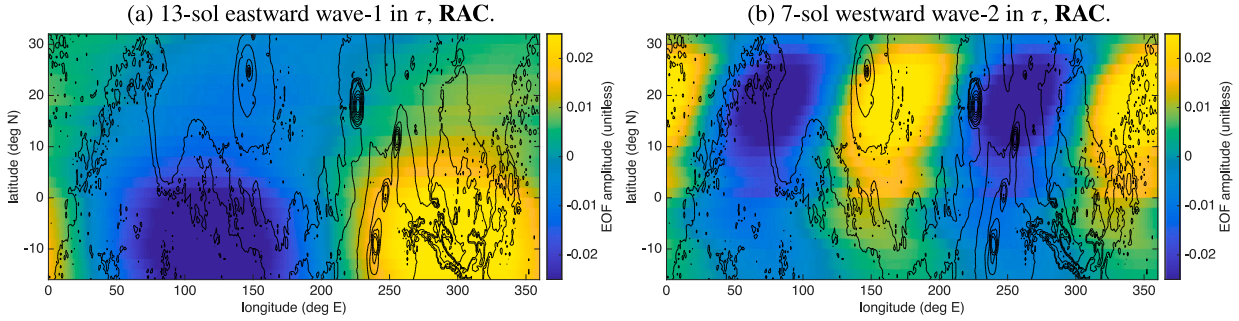


Fig. 3. First empirical orthogonal function (EOF1) of the most significant modes in the (a) K and (b) R wave bands of cloud opacity (τ) from experiment **RAC**. The dominant K and R modes correspond to an eastward-propagating wavenumber-1 wave with a 13-sol period and a westward-propagating wavenumber-2 wave with a 7-sol period, respectively.

EOF patterns do not reveal any striking Kelvin- or Rossby-wave-like features. The EOFs are more prominent in the northern hemisphere, as expected from observations. The spatial pattern of the EOFs reveals that the slow oscillations are indeed not dominated by a single wavenumber, but are characterized by two localized, oppositely signed wave packets on the opposite (i.e., western and eastern) hemispheres. The degree of separation between the oppositely signed wave packets is similar to the separation between Syrtis Major and Tharsis. The slow oscillations of such a pattern describe a slow hemispheric shift in cloud abundance, consistent with the Tropical Cloud Oscillation (TCO, Wang and González Abad, 2021). This slow hemispheric shift is further illustrated through the phase–amplitude evolution of $\imath_{ME}$ (i.e., mode $\imath$, defined in Eq. (1), determined for the ME band) shown on Fig. 8. The evolution of $\imath_{ME}$ is strikingly consistent across the 5 years of experiments, suggesting that the mode is a robust feature of the tropical dynamics rather than a mode arising from variability. The mode oscillates on multiple time scales; the mode undergoes both a 50-sol-period oscillation and an even slower cycle, resulting in only one complete cycle in its phase during $L_s = 0{-}180°$. The amplitude of the mode clearly peaks in the second half of the $L_s = 0{-}180°$ period and typically attains its maximum between phases ~270–330°. Preceding this high amplitude period is a strong local minimum a few sols prior at phase ~250°.

To better interpret the slow evolution of the dominant ME mode, we note a few useful features. Increased cloud cover above Syrtis Major

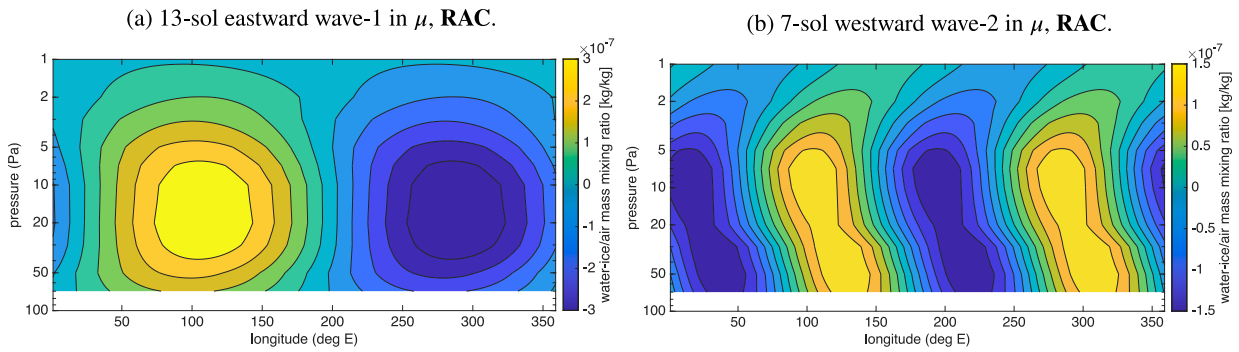


Fig. 4. Representative snapshots of the vertical structure of the meridional mean of the most significant modes in the (a) K and (b) R wave bands of cloud opacity (τ) from experiment **RAC**. The K and R modes correspond to an eastward-propagating wavenumber-1 wave with 13-sol period and a westward-propagating wavenumber-2 wave with 7-sol period, respectively. Snapshots are shown at $L_s = 150°$ during year 6 of the simulation.

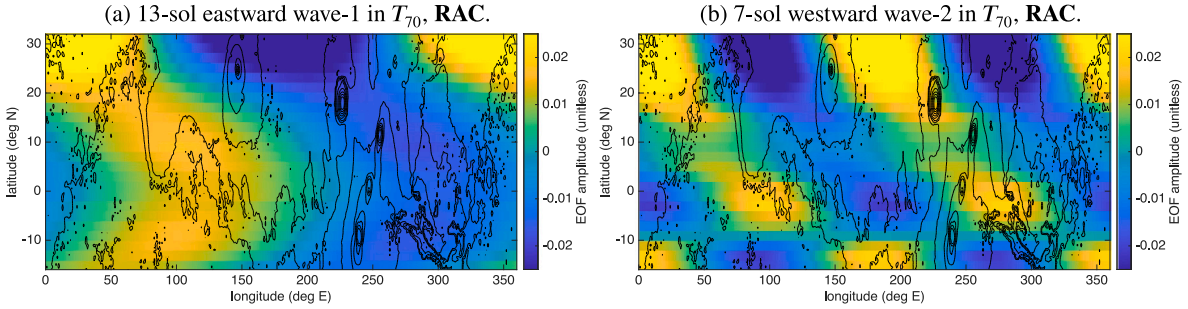


Fig. 5. First empirical orthogonal function (EOF1) of the most significant modes in the (a) K and (b) R wave bands of 70 Pa temperature (T_{70}) from experiment **RAC**. The dominant K and R modes correspond to an eastward-propagating wavenumber-1 wave with a 13-sol period and a westward-propagating wavenumber-2 wave with a 7-sol period, respectively.

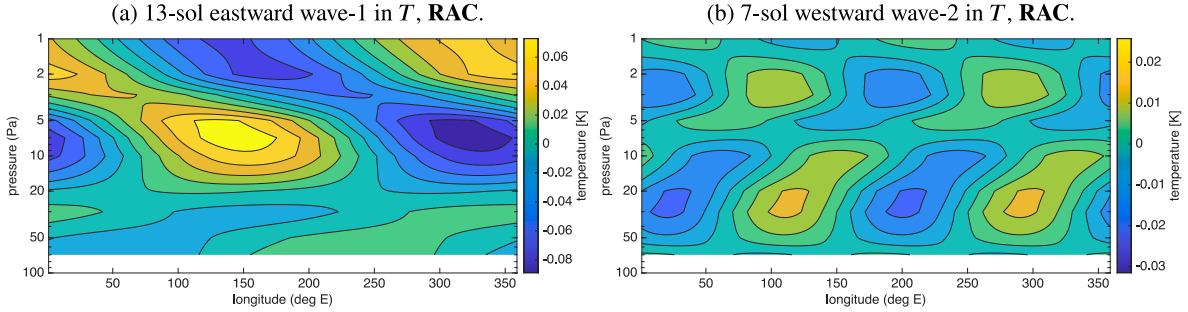


Fig. 6. Representative snapshots of the vertical structure of the meridional mean of the most significant modes in the (a) K and (b) R wave bands of temperature (T) from experiment **RAC**. The K and R modes correspond to an eastward-propagating wavenumber-1 wave with a 13-sol period and a westward-propagating wavenumber-2 wave with a 7-sol period, respectively. Snapshots are shown at $L_s = 150°$ during year 6 of the simulation.

(relative to Tharsis) occurs when the phase of ι_{ME} is either close to 0° ($PC1$ is positive and $PC2$ is zero), or 270° ($PC1$ is zero and $PC2$ is negative). Similarly, Tharsis is characterized by more clouds compared to Syrtis Major when the phase is either 180° ($PC1$ is negative and $PC2$ is zero), or 90° ($PC1$ is zero and $PC2$ is positive). The phase evolution therefore describes an increased cloud cover above Tharsis in the first half of $L_s = 0–180°$, shifting slowly towards a more cloudy Syrtis Major in the second half of this time period ($L_s = 87–180°$).

Apart from the very slow period 'oscillation' that is essentially a seasonal cycle, shorter oscillations (of periods approximately 50 sols) can also be regularly detected in ι_{ME} (e.g., a cycle occurring between phases ~250–310° in almost all years, Fig. 8). These oscillations in the second half of $L_s = 0–180°$ regularly span 60° of phase evolution of the dominating pair of modes. The limited phase evolution suggests that these 50–sol oscillations themselves do not correspond to a clear hemispheric shift. Still, they serve as a 'local' oscillation on top of a very slow period oscillation. More precisely, in a given 50–sol oscillation, the cloud cover above a specific region (e.g., Syrtis Major) may fluctuate, but is consistently high or low, depending on the representative L_s.

Finally, the vertical structure of the dominating ME-mode in the cloud field is assessed. At each vertical level (above the lowest surface pressure point), we consider the ME-band in water–ice mass mixing ratio μ. The first two EOFs and their principal components are determined, and the dominant mode ι_{ME} is constructed at each level. The mode is averaged meridionally across the tropics, and the root of the time mean square is determined; the resulting vertical structure is presented in Fig. 9. The mode expresses the highest variability above Syrtis Major. The vertical structure of the ME mode is strikingly different from the K and R modes we have determined earlier (Fig. 4). Unlike the dominant K and R modes that are most prominent around the 10 Pa level, the ME mode weakens in height consistently above 70 Pa. The decaying barotropic structure is indicative of a wave that is forced from below and is evanescent with height, as opposed to the K mode that grows with height until 20 Pa and the R mode that starts

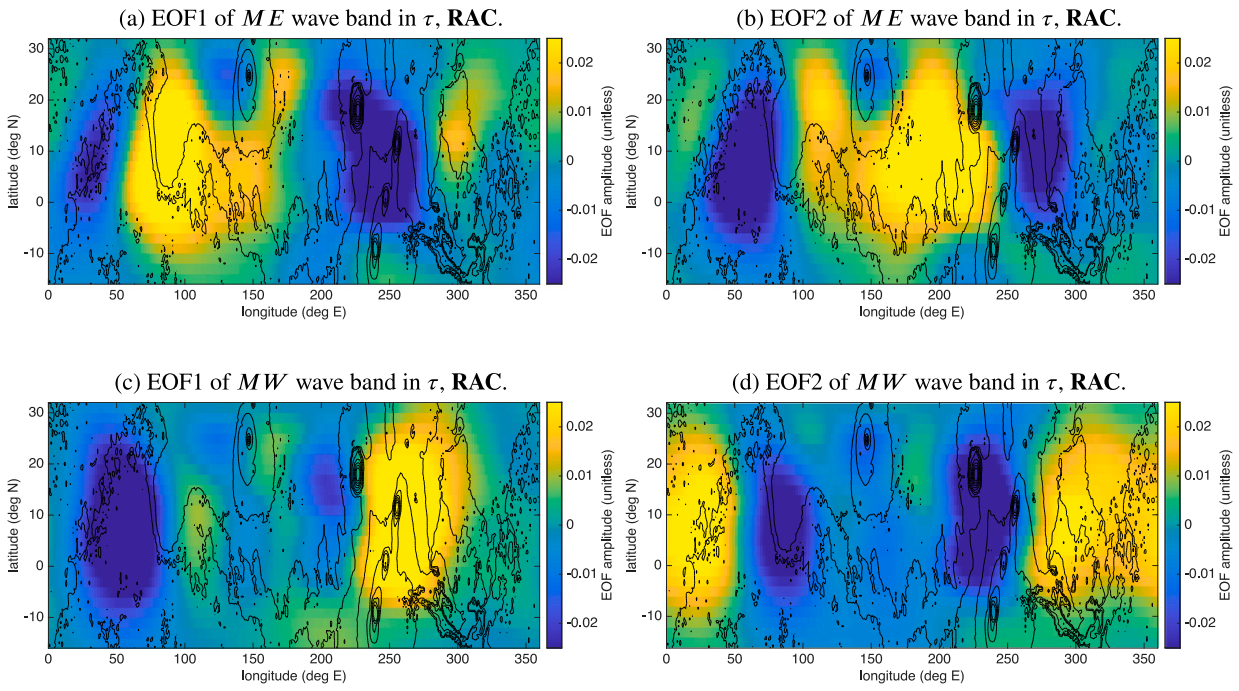


Fig. 7. Spatial structure of the leading modes of variability in the (a, b) ME and (c, d) MW wave bands in cloud opacity (τ), experiment **RAC**. The spatial patterns related to EOF1 are shown on the left (a, c), and the spatial patterns related to EOF2 are shown on the right (b, d).

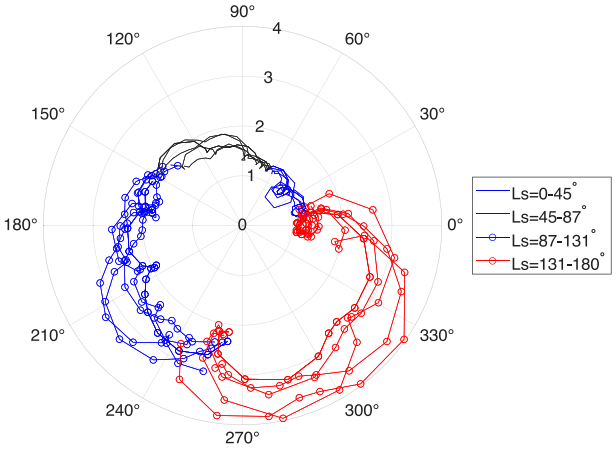


Fig. 8. Phase–amplitude evolution of the dominant wave mode ι_{ME} in the ME band of τ, 5 years total. Lines without and with circle markers correspond to the evolution in the $L_s = 0{-}87°$ and $L_s = 87{-}180°$ periods, respectively. Circle markers are displayed in 5 sol intervals.

to decay only above 5 Pa height. The numerous contrasts between the vertical structures of the slow and fast modes suggest that the cloud mass mixing ratio ME mode is fundamentally different from the K and R modes.

We further analyze the ME wave band by calculating the EOFs for 70 Pa temperature (Fig. 10(a)). Similar to our conclusions regarding the K and R modes, we see no clear relation between the spatial structures of the temperature and cloud ME modes. While the cloud ME mode attained higher amplitudes in the northern hemisphere, the 1st EOF of the temperature ME mode is more symmetric, especially at longitudes 0–250°E. The vertical structure of the temperature ME mode also expresses different patterns than that of the cloud ME mode (Fig. 10(b)). While the cloud ME mode is evanescent with height, the temperature ME mode amplitude is near zero at 50–70 Pa, and increases with height above that range. The vertical structure of the cloud ME mode was strikingly barotropic; by contrast, the temperature ME mode shows no clear barotropic behavior, and expresses both westward (30–70 Pa) and eastward (5–20 Pa) tilt with height at different altitude ranges. The 30–70 Pa westward tilt is also distinct from the eastward tilt shown for the temperature K wave. Hence, our modeling results do not suggest that the ME waves are dynamically similar to K waves, as there are qualitative differences in both spatial and vertical structure.

3.1.5. MW waves

A similar empirical orthogonal function analysis is conducted for the MW band as previously performed for the ME band. The first two leading EOFs each account for 41% of the total variance, together explaining 82% of the MW band variability. Consistent with the ME results, the spatial structures associated with the MW modes exhibit a strong Northern Hemisphere focus. While the spatial pattern of EOF1 in the MW band (Fig. 7(c)) does not appear to resemble that of EOF1 in the ME band, the two patterns become notably similar upon westward translation of the MW EOF1 by approximately 160°. A comparable relationship is evident for EOF2 (Fig. 7(d)), which likewise aligns closely with the ME EOF2 following a similar westward shift. These findings suggest that the dominant modes of variability in the ME and MW bands are closely related, potentially representing the eastward- and westward-propagating manifestations of a single underlying mode. One plausible interpretation is that these wave components arise from a standing wave structure, whose oscillation would naturally yield both eastward- and westward-propagating features with matching spatial patterns. To further investigate this hypothesis, we next examine the full M band, defined as the union of the MW and ME bands.

3.1.6. M waves

The leading empirical orthogonal function (EOF1, explaining 53% of M variability) in the τ M wave band exhibits a dipole structure characterized by oppositely signed, localized wave packets centered over Syrtis Major and the Tharsis region (Fig. 11(a)). As such, the associated principal component primarily captures the zonal asymmetry in cloud cover between these two topographic features, with minimal representation of variability outside these regions. By contrast, EOF2 (explaining 36% of M variability in the cloud τ field) is marked by

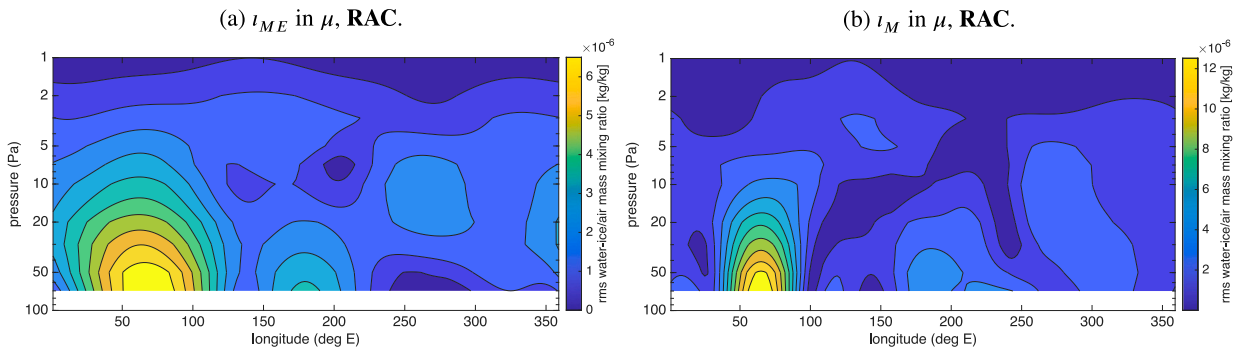


Fig. 9. Root of the time mean square of the meridionally averaged dominant ME mode ι_{ME} (a) and M mode ι_{M} (b) in water–ice mass mixing ratio (μ), experiment **RAC**.

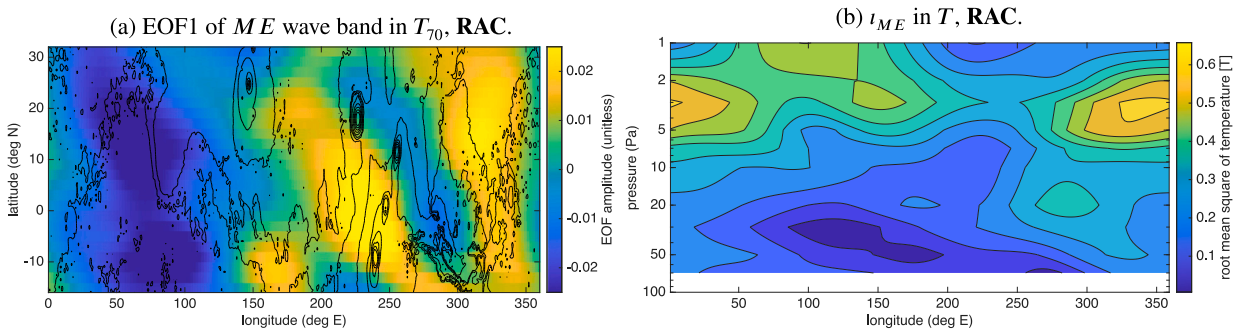


Fig. 10. Spatial and vertical structure of the leading mode of variability in the ME wave band in temperature, experiment **RAC**. The first empirical orthogonal function is displayed on (a), and the seasonal root mean square of the meridional averaged amplitude of the corresponding mode (comprising EOF1 and EOF2) is shown on (b).

negative amplitude over both Syrtis Major and Tharsis and positive amplitudes elsewhere (Fig. 11(b)). Consequently, positive anomalies in the corresponding principal component indicate enhanced cloudiness over lowland regions and reduced cloudiness over the elevated terrains. The vertical structure of the M EOF1 and EOF2 modes in μ shows almost identical patterns as the vertical structure of the ME EOF1 and EOF2 modes (Fig. 9(b)). The phase–amplitude evolution of the M EOF1 and EOF2 modes in τ (Fig. 12(a)), and the histogram of the EOF1–EOF2 phase (Fig. 12(b)) reveal three different quasi-equilibrium states where the combined EOF1–EOF2 mode is attracted to during each simulation year, at phases 60° (state 1), 200° (state 2), and 315° (state 3). For each of the three states, the amplitude of the mode undergoes oscillations with little change in phase, describing standing wave behavior. The three states are presented in Fig. 13. State 1 (L_s = 0–45° and L_s = 160° onwards) represents (compared to the mean state) a lack of clouds above Tharsis and Syrtis Major and increased cloud cover elsewhere. State 2 (around L_s = 80–110°) is characterized with increased cloud cover above Tharsis and a minor decrease above Syrtis Major. Finally, state 3 (around L_s = 125–150°) represents increased cloud cover over Syrtis Major. The TCO, a hemispheric shift between Tharsis and Syrtis Major, is therefore captured clearly as the state 2 to state 3 transition of the first two EOFs of the M band; this transition typically takes 30–40 sols each year, again consistent with the results of W24 on TCO time scales. However, the results presented here suggest that the observed hemispheric asymmetry is not necessarily attributable to a superposition of Kelvin and Rossby wave dynamics. Instead, the two leading modes of variability are more consistent with the presence of two distinct standing wave structures. From this perspective, the temporal evolution of these standing waves may be interpreted as a superposition of eastward- and westward-propagating components.

The spatial structure of the 70 Pa temperature EOF1 in the M band expresses different wave behavior from the τ modes, but shares similarities with the EOF1 in the ME band, once the M EOF1 is translated by 60° to the west (Fig. 14(a)). For the M band, the spatial pattern expresses two Rossby wave-like patterns; i.e., components that have local minima at the equator and are symmetric (at approximate longitudes 125°E and 270°E). The amplitude of the corresponding temperature EOF grows in height and peaks between 2–5 Pa (Fig. 14(b)), as in the case of the ME modes. Overall, neither the spatial nor the vertical structure of the temperature and cloud modes shows any similarity in the M band, suggesting little to no coupling between the two fields.

3.1.7. *The diurnal westward propagating wavenumber-1 tide*

Finally, we briefly present the structure of the diurnal (1-sol period) westward-propagating wavenumber-1 tide (referred to as DW1) in the temperature and cloud fields. The spatial patterns of the DW1 mode in τ and T_{70} is shown on Figs. 15(a)–15(b), and the vertical structures in μ and T are presented on Figs. 15(c)–15(d). Perhaps surprisingly, the meridional structure of the temperature and cloud modes is different; the temperature mode tilts eastward away from the equator, whereas the cloud mode tilts westward. Similarly, the vertical structures exhibit differences and similarities between the two fields. Both tides exhibit a westward tilt with height, however the temperature DW1 grows with height; however, the cloud DW1 weakens.

3.2. *Radiative effects of water–ice clouds*

In the present section, we assess tropical wave behavior in the **noRAC** simulation, which excludes radiatively active cloud feedbacks, to isolate the influence of radiative cloud–climate interactions on ACB variability. In the preceding section, tropical wave activity was examined in simulation **RAC**, which incorporated radiatively active water–ice clouds. Wavenumber–frequency spectra were computed for both the cloud field and temperature, allowing identification of key wave modes contributing to oscillations within the Aphelion Cloud Belt (ACB).

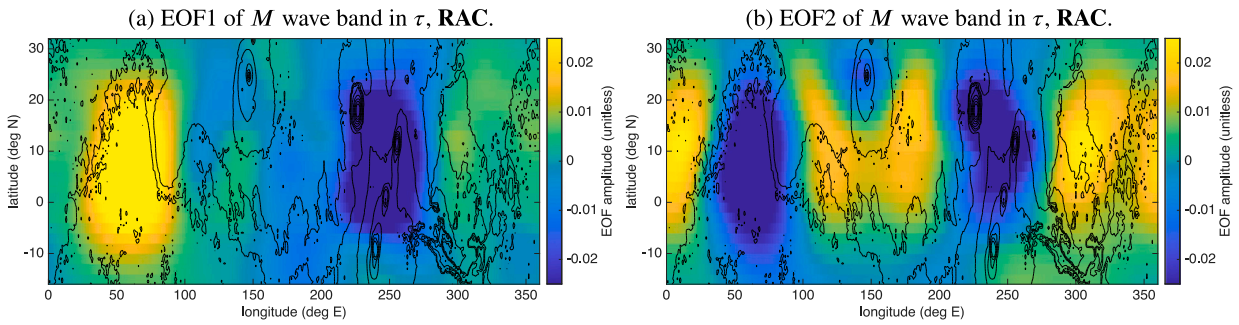


Fig. 11. Spatial structure of the leading modes of variability in the M wave band in cloud opacity (τ), experiment **RAC**. The spatial pattern related to EOF1 is shown on the left (a), and the spatial pattern related to EOF2 is shown on the right (b).

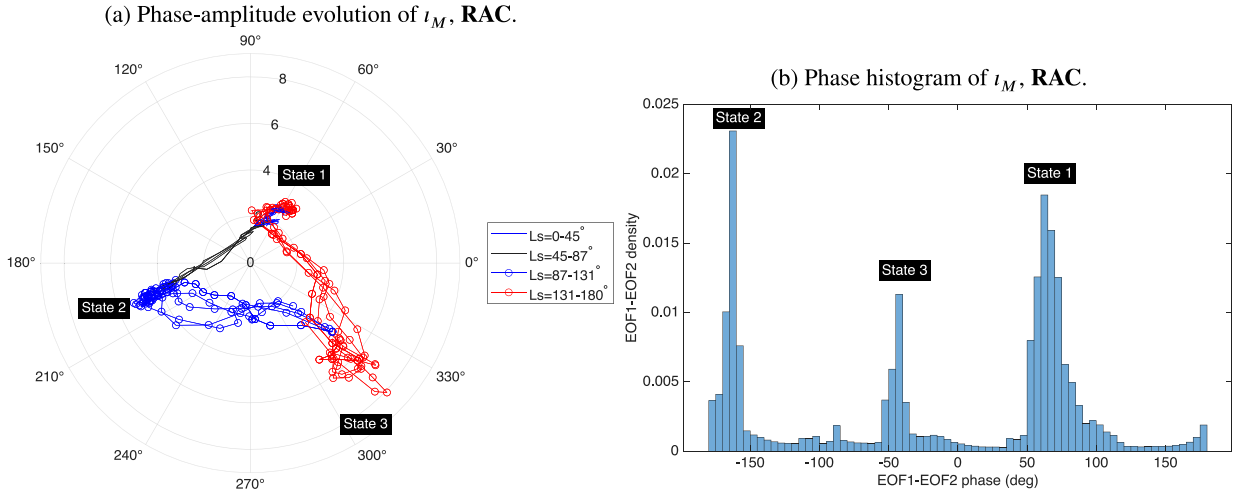


Fig. 12. (a) Phase–amplitude evolution of the dominant wave modes ι_M in the M band of τ, 5 years total in experiment **RAC**. Lines without and with circle markers correspond to the evolution in the $L_s = 0$–$87°$ and $L_s = 87$–$180°$ periods, respectively. Circle markers are displayed in 5 sol intervals. (b) Histogram depicting the fraction of time spent by the EOF1–EOF2 mode at each 5°-length phase interval.

These included fast modes (diurnal tides), moderate-period modes (K and R), and long-period modes (M), all of which modulated the ACB.

Examination of the vertical structure of the cloud field in **noRAC** (Fig. 16) reveals several notable differences relative to **RAC** (Fig. 1). Most prominently, cloud abundance is enhanced over the Tharsis region in the absence of radiative effects, whereas cloud cover is substantially reduced over Syrtis Major (Fig. 16(a)). These results suggest that radiative cloud feedbacks act to suppress cloud formation over Tharsis while enhancing it over Syrtis Major. In addition, the vertical extent of the cloud layer is considerably reduced in **noRAC**, spanning approximately 20–150 Pa (Fig. 16(b)) compared to the 3–150 Pa range observed in **RAC**, indicating a substantially thinner cloud structure in the absence of radiative forcing. Despite this reduced extent, the 70 Pa pressure level remains located near the core of the ACB and is therefore used here to examine the horizontal wave structures. Owing to the inert nature of the cloud microphysics in **noRAC**, the optical depth variable τ is not determined by the MGCM. Consequently, the water–ice cloud mass mixing ratio at 70 Pa is employed as a proxy to characterize the spatial distribution of cloud-related variability.

3.2.1. *Wavenumber–frequency spectrum*

We determine the wavenumber–frequency spectrum for μ_{70} and T_{70} (with the background removed) using the same procedure as we used for **RAC**, shown on Fig. 17. Unexpectedly, the relevant wave bands are more pronounced and readily distinguishable in **noRAC** than we reported for **RAC**. The wave spectrum associated with μ_{70} reveals a Kelvin wave-like feature, flanked by lines consistent with equivalent depths of 5.8 m and 0.36 m. Upon filtering out slower modes (i.e., cpd < 0.05), the most energetic features within the K band correspond to a wavenumber-1 wave with 18.6 sol period and a wavenumber-2 wave with 8.5 sol period, associated with an equivalent depth of approximately 1 m and 22 m, respectively. In the R band, the dominant signal is a wavenumber-1 wave with a 10.3 sol period.

3.2.2. *K and R waves*

The spatial structures of these three modes exhibit qualitative similarities to the prominent K and R modes identified in **RAC**. However, notable structural differences are also evident (Fig. 18(a–c)). Consistent with earlier findings, the first two EOFs of each analyzed wavenumber–frequency mode form a pair and explain the same variance of the mode. However, while in **RAC** a single pair of EOFs strikingly dominated the most significant wavenumber–frequency modes; here we consistently see the presence of two pairs (EOF1–EOF2 and EOF3–EOF4). More precisely, the first and second pair of EOFs account for 70% and 16% of the variance in the westward wavenumber-1, 10-sol-period wave; 82% and 10% of the variance in the eastward wavenumber-1 18.6-sol-period wave; and 60% and 25% of the variance in the eastward wavenumber-2 8.5-sol-period wave.

The EOF1 of the dominant wavenumber-1 modes (i.e., westward 10-sol-period and eastward 18.6-sol-period modes) exhibits greater amplitude in the Southern Hemisphere, whereas the EOF1 of the wavenumber-2 mode is more prominent in the Northern Hemisphere. Unlike **RAC**, the K modes now exhibit a westward tilt with latitude, in contrast to the previously observed eastward tilt in the dominant K and R modes. Nevertheless, the dominant R mode continues to exhibit

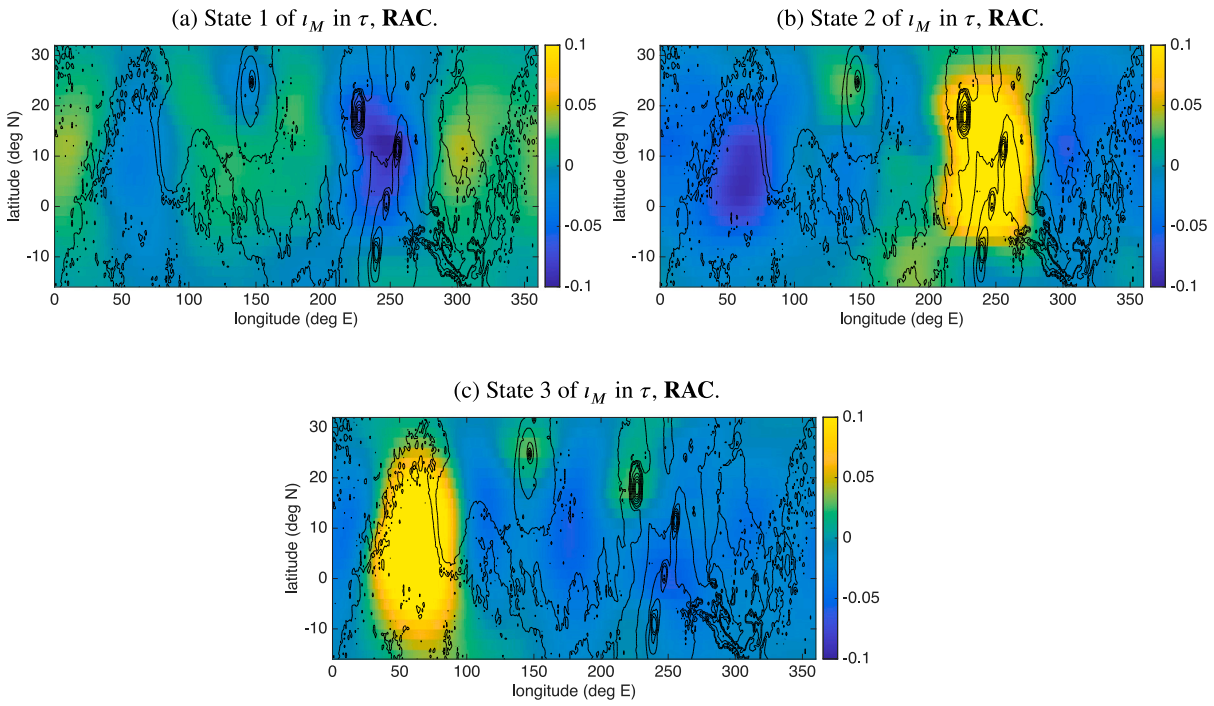


Fig. 13. Spatial structure of the three prominent states of the leading modes of variability in the M wave band in cloud opacity (τ), experiment **RAC**. The spatial pattern related to state 1 ($L_s = 0–45°$ and $L_s = 160°$ onwards) is shown in the top left panel (a), state 2 (around $L_s = 80–110°$) is shown in the top right panel (b), and state 3 (around $L_s = 125–150°$) is shown in the bottom panel (c).

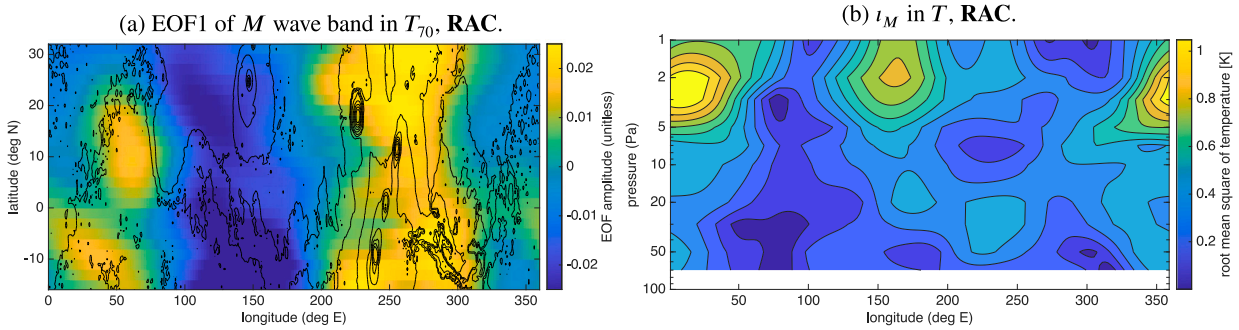


Fig. 14. Spatial and vertical structure of the leading mode of variability in the M wave band in temperature, experiment **RAC**. The first empirical orthogonal function is displayed on (a), and the seasonal root mean square of the meridional averaged amplitude of the corresponding mode (comprising EOF1 and 2) is shown on (b).

eastward tilt, indicating that the meridional structure of wave tilt is not uniformly directed away from the equator.

The second pair of modes (i.e., EOF3 and EOF4 at a given wavenumber–frequency) exhibits strong meridional asymmetry about a latitude circle that does not always coincide with the equator. The meridional structure of the three analyzed wavenumber–frequency modes differ qualitatively. Namely, the westward 10-sol-period wavenumber-1 wave exhibits eastward shift with latitude, the eastward 18.6-sol-period wavenumber-1 wave exhibits poleward shift, and the eastward 8.5-sol-period wavenumber-2 wave does not have any latitudinal dependence on its phase (apart from the phase-reversal at 7.5°N). The spatial structure of the latter is strikingly similar to wavenumber-2 Yanai wave (or mixed Rossby-gravity) patterns. According to dry equatorial wave theory, Yanai waves are expected to lie on a curve in the wavenumber–frequency spectrum that crosses the 0 zonal wavenumber line, with high-power modes on both sides.

Furthermore, the frequency of Yanai modes are expected to be similar or higher than the frequency of Kelvin and equatorial Rossby waves. Based on these expectations, it is doubtful that the asymmetric 18.6-sol-period wavenumber-1 wave would be Yanai wave, as its frequency is lower than waves in the K band and its phase being strongly latitude-dependent. While the westward 10-sol-period wavenumber-1 wave has potentially sufficiently high frequency, its phase expresses strong dependence in latitude, making it presumptuous to assume Yanai wave behavior. However, the asymmetric eastward 8.5-sol-period wavenumber-2 wave has sufficiently high frequency and its phase is not latitude-dependent, suggesting that the wave may very well be a Yanai wave.

The vertical structures, calculated as the meridional mean between 30°N and 15°S, of the dominant K and R cloud modes (comprising the first two EOFs of the wavenumber–frequency modes investigated above) are more vertically constrained (Fig. 18(d–f)), compared to those in **RAC**. The highest power R mode (i.e., 10-sol-period westward wavenumber-1) is characterized by a westward tilt with height between 70 Pa and the cloud top (10–20 Pa), similar to the wavenumber-2 R mode determined for **RAC**. The wavenumber-1 K wave exhibits barotropic behavior between 70 Pa and the near-cloud top (20 Pa), with a westward vertical tilt in the highest layers of the cloud. The wavenumber-2 K mode tilts eastward with height, although the tilt is minimal and the structure is near-barotropic.

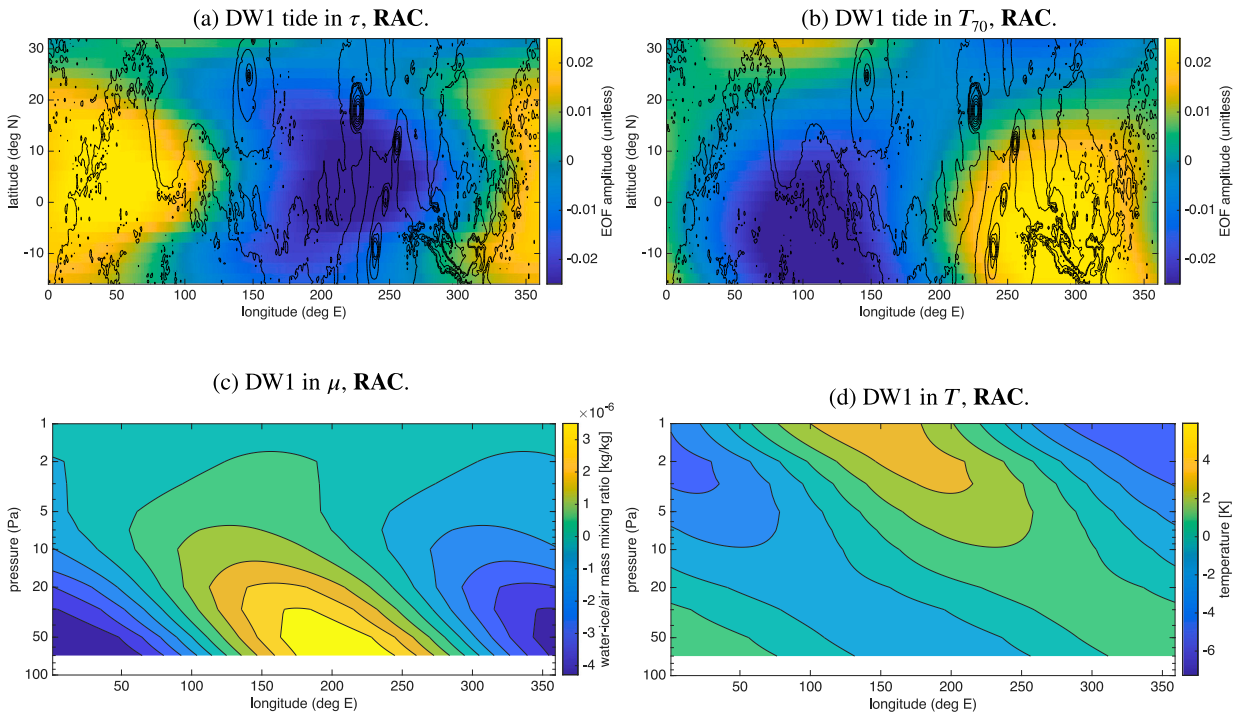


Fig. 15. Spatial and vertical structure of the DW1 tide in clouds (a, c) and temperature (b, d), experiment **RAC**. The first EOF is displayed on (a, b), and the vertical structure of the meridionally averaged amplitude is shown on (c, d) at a representative time.

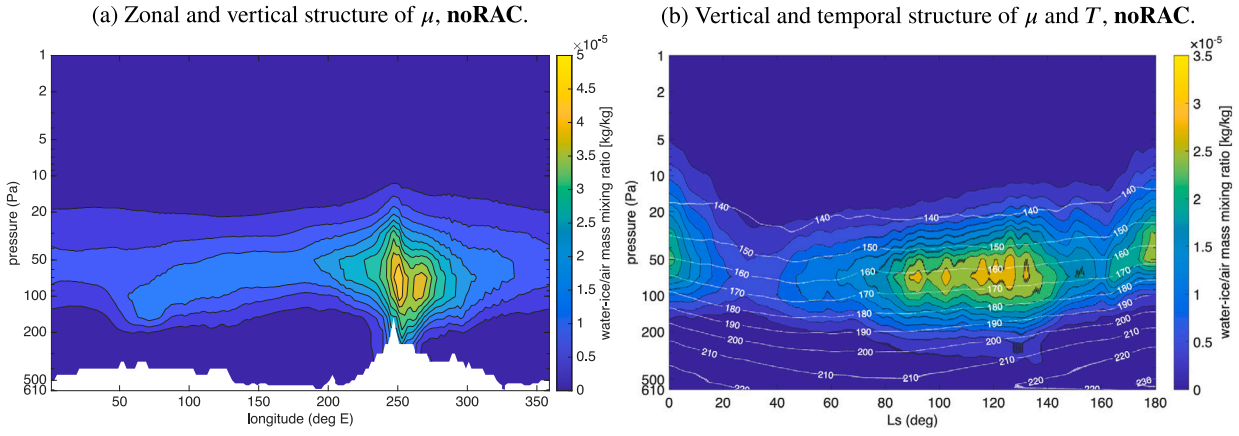


Fig. 16. Fig. 1, but for experiment **noRAC**.

The spatial and vertical structures of the temperature modes corresponding to the highest power cloud modes are displayed on Fig. 19. Similarly to the cloud modes, we find that the first two EOFs of a given wavenumber–frequency mode explain somewhat less variance than in **RAC**, although they clearly dominate the second pair of EOFs.

The first EOFs of the westward (10-sol-period) and eastward (18.6-sol-period) wavenumber-1 modes exhibit strikingly similar horizontal patterns: a local minimum at the equator and a westward phase tilt away from the equator at both hemispheres. This behavior is also present in the first EOF of the eastward 8.5-sol-period wavenumber-2 wave; each of the three dominant wave modes manifests in a qualitatively different spatial structure in temperature than what was observed in cloud structure (Fig. 18). The second pair of EOFs shows symmetric behavior about 2.5°S within the 10°N-15°S latitude band for the two K bands, suggesting Kelvin wave behavior.

Each of the three temperature modes (reconstructed from EOFs 1 and 2 of the three wavenumber–frequency modes) undergoes a qualitative change around 20–30 Pa height, coinciding with the cloud top. This coincidence suggests that the structure of the temperature mode is dynamically different within and above the cloud belt, even in the absence of radiative effects. Furthermore, while the vertical structure within the cloud belt exhibits a westward tilt with height for both wavenumber-1 waves, the vertical rate of phase change is not proportional to that observed in the cloud wave structure.

3.2.3. *M waves*

We find significant qualitative differences between the first two EOFs of the cloud M band in **noRAC** compared with those in **RAC**, including spatial structure, phase–amplitude evolution, explained variance, and vertical structure; we detail these differences in the following.

In the **noRAC** simulation, we find that the spatial structure of the first two EOFs in the M wave band (Fig. 20) differs qualitatively from those determined in **RAC**. While in **RAC** we determined an EOF1 and EOF2 that corresponded to a 'Tharsis — Syrtis Major' asymmetry and a 'highland — lowland' asymmetry, the **noRAC** experiment is characterized by EOF1 and EOF2 that describe a 'Tharsis — elsewhere'

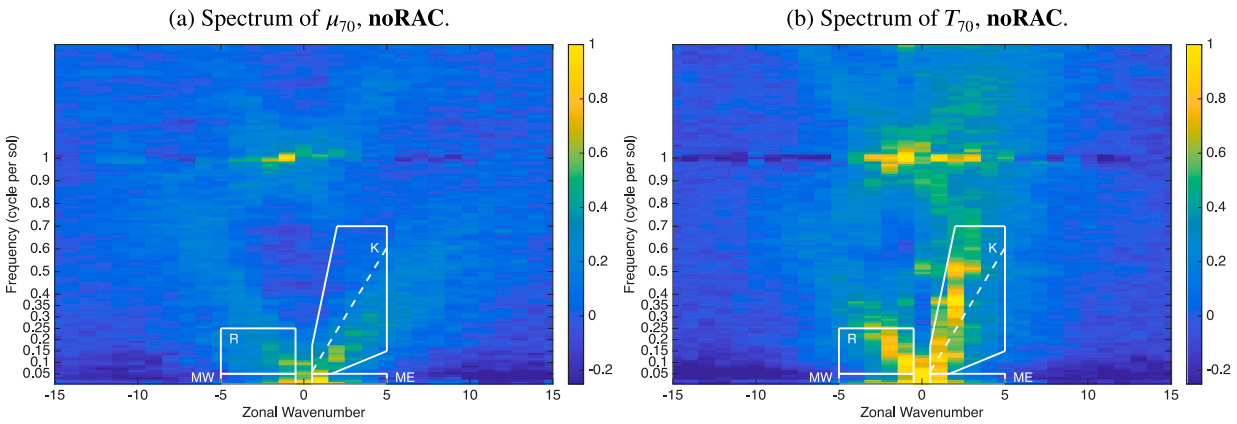


Fig. 17. Background spectrum-removed wavenumber–frequency spectra of 70 Pa water–ice mass mixing ratio μ_{70} (a) and 70 Pa temperature T_{70} (b), experiment **noRAC**. Solid white lines depict boundaries of wave bands K (long/medium eastward waves with periods longer than a sol, but less than 20 sol), R (long/medium westward waves with periods longer than a sol, but less than 20 sol), ME (slow eastward waves), and MW (slow westward waves). An additional dashed white line marks a perceived boundary for cloud Kelvin waves, corresponding to an equivalent depth of 5.8 m.

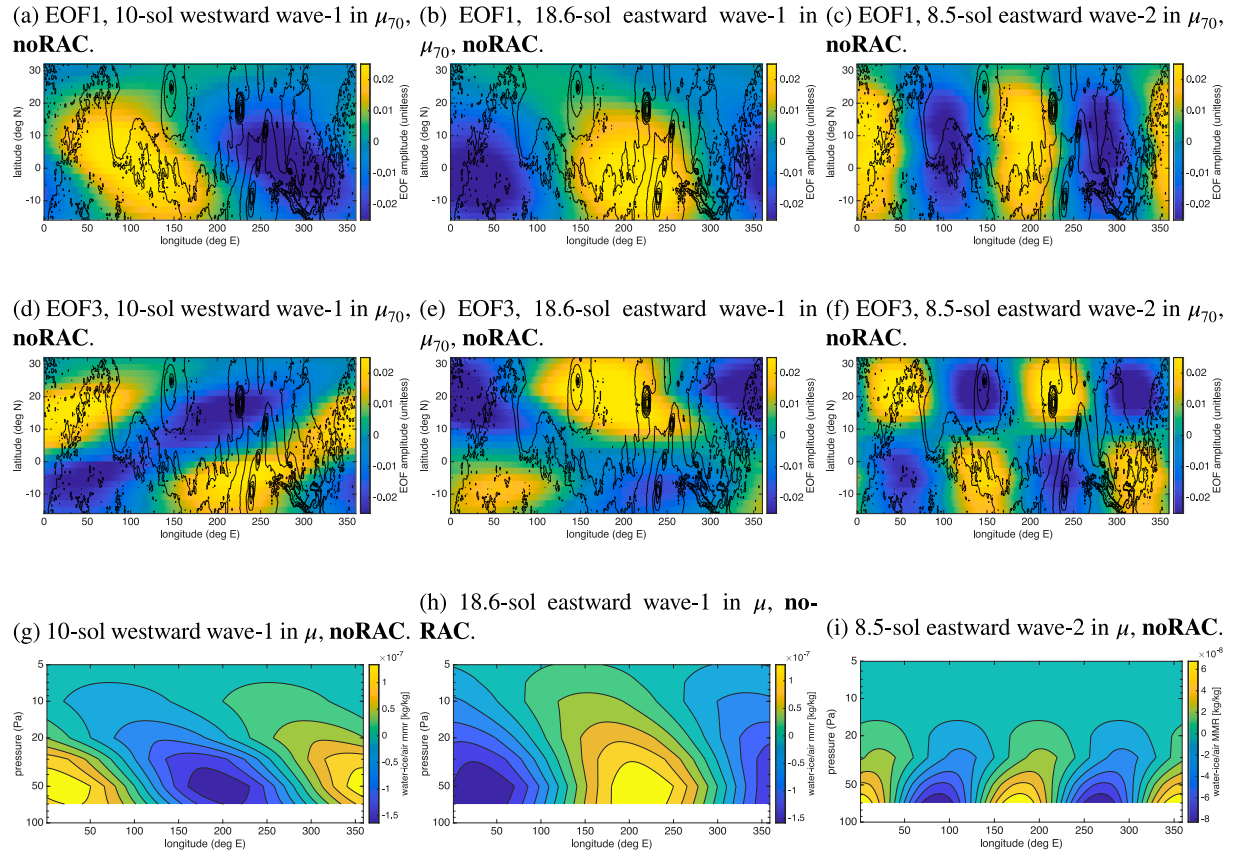


Fig. 18. Spatial (a–f) and vertical (g–i) structure of the westward 10-sol-period wavenumber-1 (a, d, g), eastward 18.6-sol-period wavenumber-1 (b, e, h), and eastward 8.5-sol-period wavenumber-2 modes (c, f, i) in water–ice cloud mass mixing ratio (μ), experiment **noRAC**. The spatial structure is illustrated through the first (a–c) and third (d–f) EOF of each mode at 70 Pa. The vertical structure (g–i) is calculated as the meridional average of the mode reconstructed from the quadrature pair EOF-1 and -2 at $L_s = 150°$ in the 6th year of the experiment.

asymmetry and a 'western Tharsis — eastern Tharsis' asymmetry, respectively. The obtained EOFs explain 60% and 23% of the total variance (within the band), respectively. Hence, the first two modes of variability still explain the vast majority of the total M band variance (83%); however, EOF1 is much more dominant over EOF2 than it was the case in **RAC** (53% and 36%). The phase–amplitude evolution of the ι_M mode (that is the combined evolution of the waves corresponding to EOF1 and EOF2) expresses further differences from the striking '3-state' structure determined in experiment **RAC** (Fig. 21). The '3-state' structure is replaced by a simple, slowly propagating mode (Fig. 21(a)) that starts the $L_s = 0–180°$ season in an equilibrium state of low cloud levels above Tharsis (around phase −170°) where it stays until approximately $L_s = 45°$, when the mode starts to undergo a slow, steady, 'anticlockwise' motion (that is, the phase of the mode is steadily increasing, without spending extended time at any phase). The anticlockwise motion is never disrupted for prolonged periods. The

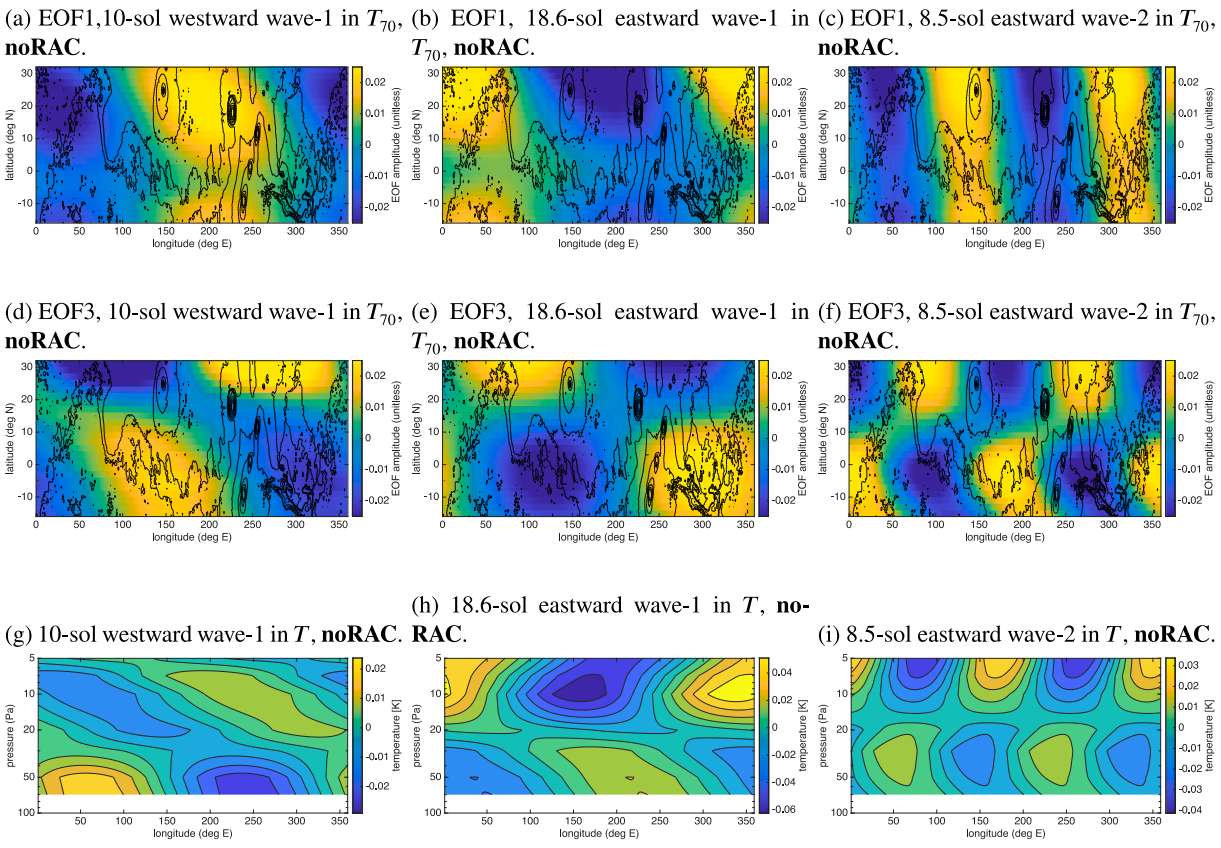


Fig. 19. Same as Fig. 18, but in temperature.

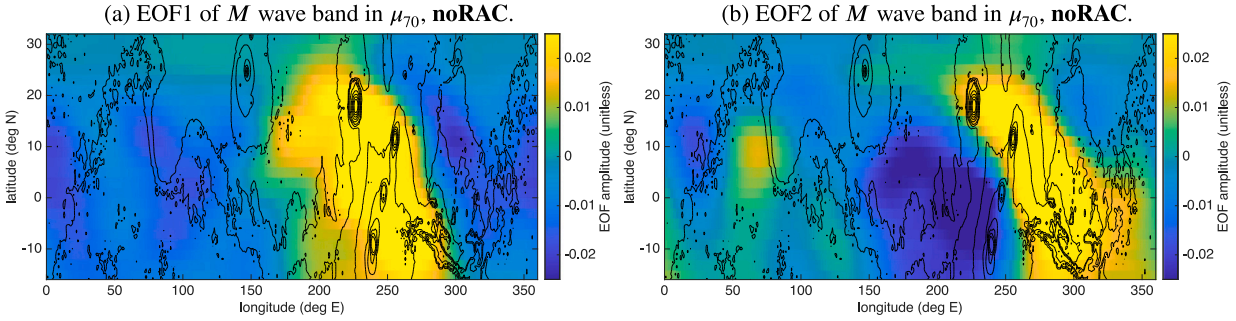


Fig. 20. Spatial structure of the leading modes of variability in the M wave band in 70 Pa water–ice mass mixing ratio (μ_{70}), experiment **noRAC**. The spatial pattern related to EOF1 is shown on the left (a), and the spatial pattern related to EOF2 is shown on the right (b).

phase histogram (Fig. 21(b)) has several shallow peaks (e.g., at broad phase intervals surrounding −135°, −45°, and 125°); however these peaks are much weaker and less focused than those obtained for the three quasi-equilibrium states in **RAC**.

Finally, the vertical structure of the ι_M mode (Fig. 22) is also qualitatively different in **noRAC** from the structure determined for **RAC**. At the same time, the majority of variability occurred over Syrtis in **RAC**, the mode in the **noRAC** experiment is characterized by high variability above Tharsis.

Overall, cloud variability of the M band when water–ice clouds are radiatively active was characterized by a '3-state' structure and a mode consisting of a 'highland — lowland' and a 'Tharsis — Syrtis Major' asymmetry, with most of the variability localized above Syrtis Major. When water–ice clouds are inert, this variability is replaced by one that is heavily focused on Tharsis, with a leading pair of modes that describe a 'Tharsis — elsewhere' and a 'western Tharsis — eastern Tharsis' asymmetry, with most of the variability being localized above Tharsis. These qualitative differences between **RAC** and **noRAC** show that radiative feedbacks of water–ice clouds exert enormous impact on long-period tropical waves, including the Tropical Cloud Oscillation.

4. Discussion

In this paper, we performed a pair of Mars GCM simulations to analyze the most significant tropical wave bands in temperature and water–ice cloud abundance during the $L_s = 0$–$180°$ season.

4.1. Summary of wave types

The wavenumber–frequency analysis and subsequent empirical orthogonal function (EOF) decomposition reveal four principal categories of wave activity in the simulated tropical cloud and temperature fields: the fast-propagating K and R modes, the slower ME and MW modes, and the diurnal westward-propagating wavenumber-1

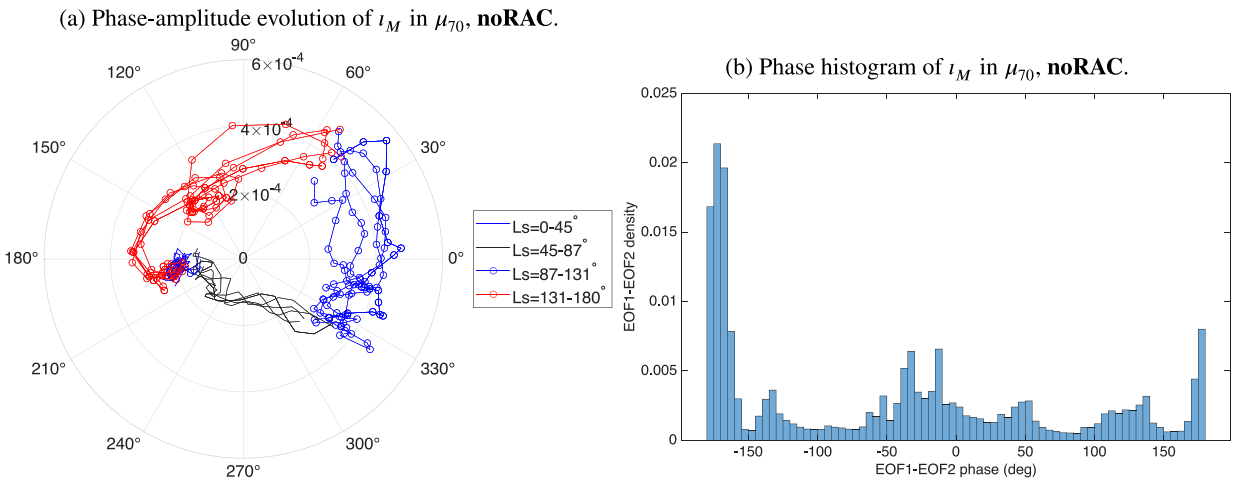


Fig. 21. (a) Phase–amplitude evolution of the dominant wave modes ι_M in the M band of μ_{70}, 5 years total in experiment **noRAC**. Lines without and with circle markers correspond to the evolution in the L_s = 0–87° and L_s = 87–180° periods, respectively. Circle markers are displayed in 5 sol intervals. (b) Histogram depicting the fraction of time spent by the EOF1–EOF2 mode at each 5°-length phase interval.

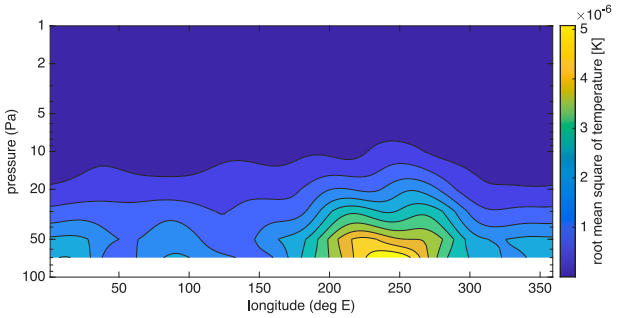


Fig. 22. Root of the time mean square of the meridionally averaged dominant M mode ι_M in water–ice mass mixing ratio (μ), experiment **noRAC**.

tide (DW1). These modes differ substantially in propagation direction, dominant period, vertical structure, and degree of coupling between the temperature and cloud fields.

The K and R modes dominate the fast eastward- and westward-propagating variability, respectively, with characteristic periods of approximately 13 and 7 sols. The K mode (eastward, wavenumber-1) is most dominant in the Southern Hemisphere. In contrast, the R mode (westward, wavenumber-2) attains greater amplitude in the northern hemisphere, indicating a hemispheric asymmetry not anticipated by classical equatorial wave theory. Vertically, the K mode exhibits a largely barotropic structure, maintaining coherence between 2 and 70 Pa, while the R mode shows a westward tilt with height between 5 and 70 Pa. Temperature analyses indicate eastward- and westward-propagating variability that broadly resembles Kelvin and equatorial Rossby waves; however, their vertical and horizontal structures deviate substantially from classical solutions. In particular, the K mode undergoes a phase reversal above 30 Pa. At the same time, the R band contains at least two overlapping components (i.e., two distinct waves at the exact wavenumber and frequency) with different vertical tilts. Together, these results suggest that while the K and R bands capture the dominant dynamical variability, the observed waves cannot be straightforwardly identified as pure Kelvin or Rossby modes.

By contrast, the ME and MW modes represent much slower, large-scale oscillations that lack clear Kelvin- or Rossby-like spatial signatures. The ME band is dominated by paired wave packets localized over the Tharsis and Syrtis Major regions, describing a slow hemispheric shift in cloud abundance that resembles the Tropical Cloud Oscillation (TCO). The vertical structure of the ME mode differs sharply from that of the K and R modes: it is barotropic in the cloud field. Still, it decays rapidly above 70 Pa, indicative of an evanescent disturbance forced from below. Temperature variability within the ME band exhibits opposing vertical behavior, with amplitudes increasing with height and alternating eastward and westward tilts across different pressure levels, further emphasizing the lack of dynamical coherence between the temperature and cloud components.

The MW band shares many features with the ME band but propagates westward. Spatially, the MW EOF patterns align closely with those of the ME band after a westward translation of roughly 160°, implying that the two are complementary manifestations of a single underlying mode. The unification of the ME and MW bands into the broader M wave band supports this interpretation, revealing a standing wave structure composed of alternating dipoles centered over Syrtis Major and Tharsis. Transitions among the three quasi-stationary M states describe the characteristic seasonal evolution of the TCO, with periodic enhancement of cloud cover shifting between the two central equatorial highlands over timescales of 30–40 sols.

Finally, the diurnal westward-propagating wavenumber-1 tide (DW1) represents the dominant short-period thermal tide. While both temperature and cloud DW1 modes exhibit a westward tilt with height, their vertical amplitudes differ: the temperature tide strengthens aloft, whereas the cloud tide weakens, suggesting that the tidal response in clouds is modulated primarily by radiative and microphysical processes rather than by direct thermodynamic forcing.

Overall, these analyses demonstrate that the modeled tropical variability arises from a spectrum of dynamical regimes. The K and R modes represent fast, vertically coherent equatorial waves with quasi-classical characteristics; the ME–MW–M modes describe slower, hemispherically asymmetric standing oscillations associated with the Tropical Cloud Oscillation; and the DW1 tide reflects the ubiquitous diurnal modulation. The lack of consistent structural correspondence between the cloud and temperature fields across all modes suggests that radiative, microphysical, and topographic influences play a critical role in shaping the observed variability, beyond the framework of idealized equatorial wave dynamics.

4.2. *Effects of radiatively active water–ice clouds*

Seasonal and zonal variations in cloud cover and temperature express strong sensitivity to whether radiative properties of water–ice clouds are switched on or off (experiments **RAC** and **noRAC**, respectively). Radiative clouds result in a balance above the two major

highland regions; Syrtis Major and Tharsis. However, inert clouds drastically reduce cloud cover over Syrtis Major. The cloud base location does not differ much between the two experiments; however, the cloud top is confined to much lower altitudes when clouds are inert. Correspondingly, inert simulations result in a much cooler atmosphere above 100 Pa; the zonal-mean 140 K isotherm is located at 20 Pa in **noRAC**, a much lower level than in **RAC** at 1–4 Pa.

The comparison between simulations with radiatively active (**RAC**) and inactive (**noRAC**) water–ice clouds reveals that cloud–radiation interactions exert substantial influence, resulting in qualitative differences in the spectrum, structure, and organization of tropical waves. In general, radiative feedbacks act to discretize and amplify spectral peaks, modify meridional and vertical phase structures, and fundamentally alter the character of the slow, large-scale M-band variability associated with the Tropical Cloud Oscillation (TCO).

In the absence of radiative effects, the wavenumber–frequency spectrum of the cloud field (μ_{70}) exhibits more clearly defined wave bands than in the **RAC** experiment. The dominant **noRAC** features correspond to eastward-propagating wavenumber-1 and -2 waves with periods of 18.6 and 8.5 sols, and a westward-propagating wavenumber-1 wave with a 10.3 sol period. These modes are energetically distinct and readily identifiable as part of a specific wave band (i.e., K or R), whereas in **RAC** the individual peaks are more prominent within the surrounding wave bands that appear much weaker and less coherent than in **noRAC**, implying that radiative coupling redistributes wave energy across nearby frequencies. The **noRAC** spectrum also reveals a wavenumber-2 mode consistent with mixed Rossby–gravity (Yanai) wave characteristics, which is less apparent when cloud–radiation interactions are included. This suggests that radiative heating by water–ice clouds suppresses some higher-frequency equatorial modes and favors slower, large-scale oscillations.

The vertical and horizontal structures of the fast K and R modes likewise differ qualitatively between the two simulations. Without radiative feedbacks, the K waves exhibit nearly barotropic vertical structures that become weakly westward tilted near the cloud top. In contrast, the R waves maintain a westward tilt with height similar to that observed in **RAC**. By comparison, radiatively active clouds promote stronger vertical coherence and enhance baroclinicity in the upper cloud layers, implying that radiative heating within the cloud deck supports upward energy propagation and modifies the phase relationship between temperature and cloud perturbations.

The most striking differences between **RAC** and **noRAC** occur within the slow M-band variability. When water–ice clouds are radiatively active, the M band exhibits the characteristic three-state evolution and spatial dipole structure associated with the TCO, featuring alternating cloudiness over Syrtis Major and Tharsis. Transitions among quasi-stationary states and strong interannual repeatability mark this regime. By contrast, the **noRAC** experiment lacks this multi-state behavior. Instead, the dominant M-mode expresses a single, slowly propagating pattern confined primarily to Tharsis, described by EOFs representing a 'Tharsis–elsewhere' and 'western–eastern Tharsis' asymmetry. The absence of a Syrtis–Tharsis dipole and the reduction of meridional coherence indicate that radiative feedbacks are essential for maintaining the hemispheric coupling and standing-wave structure characteristic of the TCO.

Vertically, the contrast is equally striking. In **RAC**, M-band variability peaks between 10 and 50 Pa and remains coherent through much of the cloud column, consistent with a radiatively driven, upward-extending disturbance. In **noRAC**, the variability is more confined to lower levels. It decays rapidly with height, implying that radiative heating by clouds not only sustains the large-scale oscillation but also enables its vertical communication throughout the tropical atmosphere. Overall, the comparison demonstrates that radiatively active water–ice clouds play an indispensable dynamical role in shaping tropical variability. By introducing vertically distributed diabatic heating and altering local static stability, cloud radiative effects (i) redistribute wave energy across nearby frequencies, leading to a discrete spectrum within the fast wave bands (K–R) instead of coherent Kelvin and Rossby wave-like wave band structures, and (ii) give rise to the distinct, multi-state Tropical Cloud Oscillation. In their absence, the system reverts to a simpler, more localized regime dominated by shallow, fast-propagating waves consistent with dry equatorial wave theory and a regionally confined variability.

4.3. Temperature–cloud decoupling

Surprisingly, the spatial patterns of temperature and cloud modes at a given wavenumber–frequency differ qualitatively across the K, R, and M wave bands, as well as in the diurnal migrating (DW1) tide. For the faster modes (periods < 20 sols), the horizontal structures of the temperature and cloud modes exhibit opposite meridional tilts. For example, the 13-sol eastward wave-1 cloud mode tilts eastward away from the equator, whereas the corresponding temperature mode tilts westward. The vertical structures of the fast cloud and temperature modes likewise display oppositely signed phase tilts within the cloud core. Notably, the phase of the temperature modes changes abruptly near the cloud top, indicating that although direct mode-to-mode coupling between clouds and temperature is weak, the mean cloud distribution nevertheless exerts an influence on the temperature modes.

The vertical structure of the slow cloud and temperature variability reveals additional mismatches. In particular, regions of enhanced variability in the slow cloud modes (e.g., above Syrtis Major) coincide with minima in temperature variability. Conversely, regions of weak variability in the slow cloud modes are associated with enhanced variability in the corresponding temperature modes.

These systematic differences between cloud and temperature modes suggest a degree of temperature–cloud decoupling, or, particularly for the slow modes, a competing control of variability by temperature and clouds. While the underlying mechanisms responsible for this behavior are not investigated here, clarifying the dynamical and thermodynamical relationships between cloud and temperature modes remains an important topic for future work.

4.4. Comparison with observations

Direct comparisons of MGCM tropical waves with observations is not straightforward due to limitations on data coverage resulting from the nature of retrieval patterns from polar orbiting spacecrafts (see e.g., Wang et al., 2024). Furthermore, comparisons with earlier research are also difficult due to a lack of careful investigation on the wavenumber–frequency properties of the ACB, since the vast majority of research focuses either on the behavior of the zonal or seasonal mean structure (Smith, 2019; Wolff et al., 2019; Giuranna et al., 2021; Guha et al., 2021b), on stationary orographic clouds (Guha et al., 2021a; Fernando et al., 2023), or on diurnal (e.g., daytime–nighttime, or 3 am–3 pm) differences (Giuranna et al., 2021; Wolff et al., 2022). In particular, we are not aware of prior publications presenting the spatial structure of cloud Kelvin and Rossby waves of periods shorter than 20 sols; as Wang et al. (2024) only investigated the horizontal structure of long period waves. Since W24 did not determine a spectrum where ghost peaks and the background was systematically removed, we are also unable to compare wavenumber–frequency spectra.

Our MGCM results share some remarkable similarities and differences with TCO patterns observed by W24. In nature (as shown by W24), the timing of the first water–ice cloud amplification above Syrtis Major occurs between $L_s = 135–150°$ each MY investigated, with some variability in the exact initial date of the amplification. In our simulations, the slow ι_M mode enters state 3 around $L_s = 130°$ and amplifies shortly after; the timing is therefore consistent with observations. However, W24 showed that in some years there may be a second amplification occurring shortly after $L_s = 150°$. This

second amplification is not captured by the evolution of the ι_M mode in the MGCM, suggesting that the second amplification may either be driven by faster waves or the MGCM may be missing relevant physics specifications. Correspondingly, the TCO might decompose into a 'slow TCO' and a 'fast TCO', with the fast TCO not captured by the MGCM and the slow TCO being represented by a standing wave-induced transition between states 2 and 3.

Some information on Kelvin and Rossby waves and on the TCO may also be inferred from surface lander observations near the equator. Clearly, one should not simply assume that waves in the cloud belt project onto surface-level variables. Nonetheless, Battalio et al. (2022) determined a 25-sol period oscillation that is consistent across pressure, temperature, relative humidity, zonal and meridional winds at surface level at Mars 2020 in Jezero crater. Since the location of Jezero crater falls within the high amplitude region of EOF1 in the M band, TCO-related oscillations may be observed at Mars 2020. Further 18-sol, 7-sol, and 4.5-sol period oscillations (potentially linked to Kelvin and Rossby waves) were also determined, albeit not in every variable analyzed.

Finally, Mastcam-Z's (on Perseverance Rover, Mars 2020) visible aerosol optical depth record (Lemmon, 2025) has determined a rapid increase in water–ice clouds above Jezero around $L_s = 142{-}145°$ in each of MY 36, 37, and 38 (Lemmon et al., 2025). The timing and location coincides with an amplified state 3 of M band variability.

4.5. Strengths and limitations of the MY 30 dust scenario

Each simulation year was forced with the same dust scenario, corresponding to Mars Year (MY) 30. The MY 30 dust scenario was chosen because it represents a typical MY over $L_s = 0{-}180°$, with peak dust opacity around $L_s = 170°$, late in the studied time interval. The lack of interannual dust variability in our experiments is therefore a consequence of the model setup and has advantages and disadvantages for studying the tropical wave modes. The main benefits that motivated our selection of the aforementioned dust cycle stem from the impacts of strong dust events. Namely, vigorous atmospheric dust activity modifies the temperature structure through radiative feedbacks, potentially leading to specific wave modes being suppressed or amplified during the duration of the dust activity. Therefore, calculating temperature wave spectra over multiple years that experience different dust forcing might result in certain wave modes losing significance.

Furthermore, higher temperatures (during strong dust events) suppress the formation of water–ice clouds, weakening wave amplitudes and power in the interannually averaged wave spectrum. Hence, the described dust forcing helps to characterize significant wave bands with more precision. On the other hand, this choice of dust forcing has its consequential shortcomings. The resulting wave spectra are specific to MY 30 conditions, and their dust forcing might suppress or amplify specific wave modes, both in temperature and clouds, that are otherwise key modes of variability on Mars in other years. Hence, our model configuration allows us to determine the general positions of the key wave bands and specify key wave modes in the wavenumber–frequency spectrum, but, on the downside, specific wave modes relevant in some MYs might be systematically suppressed.

4.6. Discussion on the background spectrum

The wave-spectrum calculation included the removal of a background spectrum. The determined background spectrum is dominated by wave energy at low frequency (typically referred to as a 'red' spectrum) and at integer values of cycles per sol (cps). The red spectrum is a well-known feature of tropical waves on Earth; however, the high energy observed around integer values of cps is absent from the tropical wave spectrum. These bands of high energy are centered on and attributed to the thermal tides of Mars. While the background spectrum removal is standard and widely used in studies of Earth's tropical waves, the only research (Wang et al., 2024) on Mars' tropical wave spectrum prior to our work did not remove the background spectrum. While the work of W24 argued that the nature of MRO observations is the culprit behind their alternative method, we encourage future observational studies to determine the background spectrum and explain in more detail why this method is not a good one. We also encourage future studies to consider data from other spacecraft (e.g. from the Emirates Mars Mission) to help determine a background-removed spectrum.

4.7. Discussion on reanalysis datasets

With NASA's recent shift to focus on its Moon 2 Mars program, Mars weather forecast capabilities will be necessary for operational support. There are three publicly available reanalysis datasets currently. Two of them, OpenMARS (Holmes et al., 2020) and MACDA (Montabone et al., 2014), are produced with a GCM configuration that does not include radiatively active water–ice clouds, while the GCM configuration that EMARS is produced from does (Greybush et al., 2019). Our results indicate qualitative and quantitative differences between wave bands obtained from simulations with radiatively active or inert water–ice clouds. These differences may not be directly applicable to reanalysis datasets, since the reanalyses are built on measurements, and the measured temperatures naturally experience radiative effects. Therefore, radiative coupling is built in the reanalysis through the observations. However, because observations are limited to two local times a day, a reanalysis without radiatively active water–ice clouds may not reproduce all the natural variability of tropical waves. These limitations should be carefully considered if one is attempting to assess tropical waves on Mars using OpenMARS or MACDA.

4.8. Future work

Our results raise several open questions that could be investigated through observations, further GCM modeling, or simplified theoretical analysis. Most crucially, observations should be used to determine the most significant wave bands after background subtraction. Then, the long-period waves that form the TCO can be more carefully interpreted, and it can be determined whether they are part of a Kelvin or Rossby wave band or of a separate wave structure. We encourage further GCM modeling to analyze how tropical wave bands respond to different dust-forcing (or scenarios) and to also design idealized experiments that allow focusing on the long-period waves that form the TCO. Additionally, since the reanalysis datasets OpenMARS and MACDA do not include radiatively active water–ice clouds, whereas EMARS does, it might provide a worthwhile comparison of the tropical wave bands in the two reanalysis datasets. Even though the two reanalyses are produced with different models and assimilation schemes, such a comparison could provide insight into the importance of including radiatively active water–ice clouds in determining and predicting tropical wave bands. An even more insightful comparison would be to run a given reanalysis with and without radiatively active water–ice clouds. Still, such a project would depend on whether the developers of the reanalyses deem it worthy of their resources. Finally, we encourage the development of a minimal linear model that can describe coupling between cloud-bottom and surface temperatures via radiative effects, and the derivation of a dispersion relation for radiatively coupled equatorial waves.

5. Conclusions

The analyses presented here, based on Mars Global Climate Model (MGCM) simulations, demonstrate that the tropical variability of Mars' Aphelion Cloud Belt arises from a superposition of fast waves with similarities and differences from classical equatorial waves, and slow, large-scale oscillations that are strongly modulated by cloud–radiation interactions. The main results can be summarized as follows:

- Fast (1–20-sol period) waves in the cloud field are dominated by eastward-propagating K modes and westward-propagating R modes; the highest power K and R modes exhibit coherent wave-1 and wave-2 structures with periods of 7–13 sols.
- The K and R modes share several characteristics with Kelvin- and Rossby-type dynamics, respectively, and occupy a band on the wavenumber–frequency spectrum that matches expectations of Kelvin and Rossby waves based on linear theory, particularly when clouds are inert. However, the modes obtained from the MGCM experiments deviate from idealized theory through north–south hemispheric asymmetry and vertically varying phase structures.
- If clouds are inert, continuous wave bands are present on the wavenumber–frequency spectrum, consistent with expectations regarding Kelvin and Rossby wave band appearance. When clouds are radiatively active, these continuous bands are suppressed and are instead dominated by a discrete set of high power modes.
- Long period cloud variability is considered by analyzing the M wave band, consisting waves with 20 sol < period and wavenumbers 1–5 (both eastward and westward). When clouds are radiatively active, two leading modes of variability dominate the M band. These two modes correspond to a Tharsis–Syrtis Major asymmetry, and a highland–lowland asymmetry.
- With radiatively active water–ice clouds, the two leading modes of M band variability represent standing waves and may attain three quasi-equilibrium states during the $L_s = 0–180°$ period. The two modes may enter a quasi-equilibrium state and spend prolonged time in that configuration; upon leaving the state, a swift transition takes place to enter the subsequent quasi-equilibrium state.
- The transition between quasi-equilibrium states 2 and 3 is interpreted as the Tropical Cloud Oscillation (TCO), which only emerges when water–ice clouds are radiatively active.
- In the absence of cloud radiative effects, the M band variability becomes localized and is dominated by vertically shallow disturbances centered over Tharsis. Therefore, cloud–climate radiative feedbacks qualitatively modulate long period cloud waves.
- Several lines of evidence suggest that the TCO is not driven by Kelvin and/or Rossby waves in the MGCM. First, the location of the Kelvin and Rossby wave associated bands in **noRAC** are clearly separate from the M band with no overlap, suggesting that Kelvin and Rossby waves do not appear at periods longer than 20 sols. Second, when clouds are radiatively active the spatial patterns of the leading modes of variability in the M band are centered about a fixed latitude; whereas K and R cloud waves express north–south asymmetry. Furthermore, the dominant K and R modes are vertically coherent, extending to the cloud top; however, the M modes are vertically trapped. Finally, M band wave variability is shown to be driven by standing wave patterns.
- The analysis provides no evidence for a coherent coupling between temperature and cloud variability. For a given wavenumber–frequency component, the horizontal and vertical structures of the cloud and temperature fields are qualitatively distinct. This lack of correspondence applies to both the fast K and R modes as well as to the longer-period variability associated with the M band.

Together, these MGCM results indicate that the radiative effects of clouds are integral to the dynamical organization of tropical variability; the simulated Aphelion Cloud Belt represents not merely a passive tracer of atmospheric motion but is an active participant in the maintenance of Mars' tropical wave spectrum and seasonal variability.

CRediT authorship contribution statement

Márton Mester: Writing – original draft, Software, Methodology, Investigation, Formal analysis, Conceptualization. **R. John Wilson:** Writing – review & editing, Validation, Investigation. **Melinda A. Kahre:** Writing – review & editing, Project administration.

Declaration of competing interest

The authors declare that they have no known competing financial interests or personal relationships that could have appeared to influence the work reported in this paper.

Acknowledgments

MM is funded by the NASA Postdoctoral Program. Support for this research was also provided by NASA's Planetary Science Division Research Program, through the Mars Climate Modeling Center (MCMC) Internal Scientist Funding Model (ISFM) work package at Ames Research Center. The authors would like to thank two anonymous reviewers for their careful assessment and feedback that helped improve the paper, and Rei Ueyama for discussions on early versions of the manuscript.

Data availability

Dataset link: https://doi.org/10.5281/zenodo.17725947

Radiatively Coupled Equatorial Waves in Mars' Aphelion Cloud Belt: Wavenumber--Frequency Analysis in Mars GCM Simulations (Original data) (zenodo)

References

Battalio, J.M., Martínez, G., Newman, C., de la Torre Juarez, M., Sánchez-Lavega, A., Víudez-Moreiras, D., 2022. Planetary waves traveling between mars science laboratory and mars 2020. Geophys. Res. Lett. 49, e2022GL100866. http://dx.doi.org/10.1029/2022GL100866.

Bertrand, T., Wilson, R.J., Kahre, M.A., Urata, R., Kling, A., 2020. Simulation of the 2018 global dust storm on mars using the NASA Ames mars GCM: A multitracer approach. J. Geophys. Res.: Planets 125, e2019JE006122. http://dx.doi.org/10.1029/2019JE006122.

Clancy, R., Grossman, A., Wolff, M., James, P., Rudy, D., Billawala, Y., Sandor, B., Lee, S., Muhleman, D., 1996. Water vapor saturation at low altitudes around mars aphelion: A key to mars climate? Icarus 122, 36–62. http://dx.doi.org/10.1006/icar.1996.0108.

Fernando, A.M., Wolff, M.J., Forget, F., 2023. Seasonal variations of orographic clouds on mars with mro/marci observations and the mars planetary climate model. Icarus 400, 115559. http://dx.doi.org/10.1016/j.icarus.2023.115559.

Frank, W.M., Roundy, P.E., 2006. The role of tropical waves in tropical cyclogenesis. Mon. Weather Rev. 134, 2397–2417. http://dx.doi.org/10.1175/MWR3204.1.

Giuranna, M., Wolkenberg, P., Grassi, D., Aronica, A., Aoki, S., Scaccabarozzi, D., Saggin, B., Formisano, V., 2021. The current weather and climate of mars: 12 years of atmospheric monitoring by the planetary fourier spectrometer on mars express. Icarus 353, 113406. http://dx.doi.org/10.1016/j.icarus.2019.113406, from Mars Express to Exomars.

Greybush, S.J., Kalnay, E., Wilson, R.J., Hoffman, R.N., Nehrkorn, T., Leidner, M., Eluszkiewicz, J., Gillespie, H.E., Wespetal, M., Zhao, Y., Hoffman, M., Dudas, P., McConnochie, T., Kleinböhl, A., Kass, D., McCleese, D., Miyoshi, T., 2019. The ensemble mars atmosphere reanalysis system (EMARS) version 1.0. Geosci. Data J. 6, 137–150. http://dx.doi.org/10.1002/gdj3.77.

Guha, B.K., Panda, J., Arya, A., 2021a. Characteristic features of water ice clouds over olympus and arsia mons using mom and mro observations. Planet. Space Sci. 196, 105155. http://dx.doi.org/10.1016/j.pss.2020.105155.

Guha, B.K., Panda, J., Wu, Z., 2021b. Observation of aphelion cloud belt over Martian tropics, its evolution, and associated dust distribution from MCS data. Adv. Space Res. 67, 1392–1411. http://dx.doi.org/10.1016/j.asr.2020.11.010.

Haberle, R.M., Kahre, M.A., Hollingsworth, J.L., Montmessin, F., Wilson, R.J., Urata, R.A., Brecht, A.S., Wolff, M.J., Kling, A.M., Schaeffer, J.R., 2019. Documentation of the NASA/Ames legacy mars global climate model: Simulations of the present seasonal water cycle. Icarus 333, 130–164. http://dx.doi.org/10.1016/j.icarus.2019.03.026.

Haertel, P.T., Kiladis, G.N., Denno, A., Rickenbach, T.M., 2008. Vertical-mode decompositions of 2-day waves and the Madden–Julian oscillation. J. Atmos. Sci. 65, 813–833. http://dx.doi.org/10.1175/2007JAS2314.1.

Harris, L., Chen, X., Putman, W., Zhou, L., Chen, J.H., 2021. A scientific description of the gfdl finite-volume cubed-sphere dynamical core. In: NOAA Technical Memorandum OAR GFDL ; 2021-001. http://dx.doi.org/10.25923/6nhs-5897.

Hinson, D.P., Wilson, R.J., 2004. Temperature inversions, thermal tides, and water ice clouds in the Martian tropics. J. Geophys. Res.: Planets 109, http://dx.doi.org/10.1029/2003JE002129.

Holmes, J.A., Lewis, S.R., Patel, M.R., 2020. Openmars: A global record of Martian weather from 1999 to 2015. Planet. Space Sci. 188, 104962. http://dx.doi.org/10.1016/j.pss.2020.104962.

Kahre, M., Hollingsworth, J., Haberle, R., Wilson, R., 2015. Coupling the mars dust and water cycles: The importance of radiative-dynamic feedbacks during northern hemisphere summer. Icarus 260, 477–480. http://dx.doi.org/10.1016/j.icarus.2014.07.017, URL https://www.sciencedirect.com/science/article/pii/S0019103514003832.

Kahre, M.A., Urata, R.A., Wilson, R.J., Hartwick, V., Wolff, M.J., 2024. Modeling the water cycle with the NASA Ames FV3-based mars global climate model. Tenth Int. Conf. Mars URL https://www.hou.usra.edu/meetings/tenthmars2024/pdf/3424.pdf.

Kiladis, G.N., Wheeler, M.C., Haertel, P.T., Straub, K.H., Roundy, P.E., 2009. Convectively coupled equatorial waves. Rev. Geophys. 47, http://dx.doi.org/10.1029/2008RG000266.

Lemmon, M., 2025. The perseverance rover's mastcam-z visible aerosol optical depth record. http://dx.doi.org/10.17632/gktjp9jptb.1.

Lemmon, M.T., Wolff, M.J., Bell, J.F., Hayes, A., Maki, J., 2025. The perseverance rover's mastcam-z visible aerosol optical depth recor. AGU25 URL https://agu.confex.com/agu/agu25/meetingapp.cgi/Paper/1911427.

Madeleine, J.B., Forget, F., Millour, E., Navarro, T., Spiga, A., 2012. The influence of radiatively active water ice clouds on the Martian climate. Geophys. Res. Lett. 39, http://dx.doi.org/10.1029/2012GL053564.

Matthews, A.J., 2000. Propagation mechanisms for the Madden-Julian oscillation. Q. J. R. Meteorol. Soc. 126, 2637–2651. http://dx.doi.org/10.1002/qj.49712656902.

Montabone, L., Forget, F., Millour, E., Wilson, R., Lewis, S., Cantor, B., Kass, D., Kleinböhl, A., Lemmon, M., Smith, M., Wolff, M., 2015. Eight-year climatology of dust optical depth on mars. Icarus 251, 65–95. http://dx.doi.org/10.1016/j.icarus.2014.12.034, dynamic Mars.

Montabone, L., Marsh, K., Lewis, S.R., Read, P.L., Smith, M.D., Holmes, J., Spiga, A., Lowe, D., Pamment, A., 2014. The mars analysis correction data assimilation (macda) dataset v1.0. Geosci. Data J. 1, 129–139. http://dx.doi.org/10.1002/gdj3.13.

Putzig, N.E., Mellon, M.T., 2007. Apparent thermal inertia and the surface heterogeneity of mars. Icarus 191, 68–94. http://dx.doi.org/10.1016/j.icarus.2007.05.013.

Richardson, M.I., Wilson, R.J., Rodin, A.V., 2002. Water ice clouds in the Martian atmosphere: General circulation model experiments with a simple cloud scheme. J. Geophys. Res.: Planets 107, 2–1–2–29. http://dx.doi.org/10.1029/2001JE001804.

Sánchez-Lavega, A., Larsen, E., del Rio-Gaztelurrrutia, T., Hernández-Bernal, J., Ordóñez Etxebarría, I., Hueso, R., Bertrand, T., Lemmon, M., Juarez, M.d.l. T., Martínez, G.M., Munguira, A., Rodríguez-Manfredi, J.A., Harri, A.M., Pla-García, J., Toledo, D., Newman, C., 2025. Martian atmospheric disturbances from orbital images and surface pressure at jezero crater, mars, during Martian year 36. J. Geophys. Res.: Planets 130, e2024JE008565. http://dx.doi.org/10.1029/2024JE008565.

Simmons, A.J., Burridge, D.M., 1981. An energy and angular-momentum conserving vertical finite-difference scheme and hybrid vertical coordinates. Mon. Weather Rev. 109, 758–766. http://dx.doi.org/10.1175/1520-0493(1981)109<0758:AEAAMC>2.0.CO;2.

Smith, M.D., 2019. Local time variation of water ice clouds on mars as observed by themis. Icarus 333, 273–282. http://dx.doi.org/10.1016/j.icarus.2019.06.009.

Steele, L.J., Lewis, S.R., Patel, M.R., 2014. The radiative impact of water ice clouds from a reanalysis of mars climate sounder data. Geophys. Res. Lett. 41, 4471–4478. http://dx.doi.org/10.1002/2014GL060235.

Tyler, D., Barnes, J.R., 2014. Atmospheric mesoscale modeling of water and clouds during northern summer on mars. Icarus 237, 388–414. http://dx.doi.org/10.1016/j.icarus.2014.04.020, URL https://www.sciencedirect.com/science/article/pii/S0019103514002127.

Wang, H., Battalio, M., Huber, Z., 2020. MRO MARCI mars daily global maps V2. http://dx.doi.org/10.7910/DVN/U3766S.

Wang, H., González Abad, G., 2021. Cloud masks derived from the mars daily global maps and an application to the tropical cloud belt on mars. Geosciences 11, http://dx.doi.org/10.3390/geosciences11080324.

Wang, H., Ingersoll, A.P., 2002. Martian clouds observed by mars global surveyor mars orbiter camera. J. Geophys. Res.: Planets 107, 8–1–8–16. http://dx.doi.org/10.1029/2001JE001815.

Wang, H., Richardson, M.I., Toigo, A.D., Newman, C.E., 2024. Large scale oscillations in the Martian tropical cloud belt. J. Geophys. Res.: Planets 129, e2024JE008479. http://dx.doi.org/10.1029/2024JE008479, e2024JE008479 2024JE008479.

Welch, P., 1967. The use of fast fourier transform for the estimation of power spectra: A method based on time averaging over short, modified periodograms. IEEE Trans. Audio Electroacoust. 15, 70–73. http://dx.doi.org/10.1109/TAU.1967.1161901.

Wheeler, M.C., Hendon, H.H., 2004. An all-season real-time multivariate mjo index: Development of an index for monitoring and prediction. Mon. Weather Rev. 132, 1917–1932. http://dx.doi.org/10.1175/1520-0493(2004)132<1917:AARMMI>2.0.CO;2.

Wheeler, M., Kiladis, G.N., 1999. Convectively coupled equatorial waves: Analysis of clouds and temperature in the wavenumber–frequency domain. J. Atmos. Sci. 56, 374–399. http://dx.doi.org/10.1175/1520-0469(1999)056<0374:CCEWAO>2.0.CO;2.

Wilson, R.J., Guzewich, S.D., 2014. Influence of water ice clouds on nighttime tropical temperature structure as seen by the mars climate sounder. Geophys. Res. Lett. 41, 3375–3381. http://dx.doi.org/10.1002/2014GL060086.

Wilson, R.J., Lewis, S.R., Montabone, L., Smith, M.D., 2008. Influence of water ice clouds on Martian tropical atmospheric temperatures. Geophys. Res. Lett. 35, http://dx.doi.org/10.1029/2007GL032405.

Wilson, R.J., Millour, E., Navarro, T., Forget, F., Kahre, M.A., 2014. GCM simulations of aphelion season tropical cloud and temperature structure. In: Mars Atmosphere: Modeling and Observations, 5th International Workshop. Oxford, UK, URL https://www-mars.lmd.jussieu.fr/oxford2014/abstracts/wilson_clouds_oxford2014.pdf.

Wilson, R.J., Neumann, G.A., Smith, M.D., 2007. Diurnal variation and radiative influence of Martian water ice clouds. Geophys. Res. Lett. 34, http://dx.doi.org/10.1029/2006GL027976.

Wolff, M.J., Clancy, R.T., Kahre, M.A., Haberle, R.M., Forget, F., Cantor, B.A., Malin, M.C., 2019. Mapping water ice clouds on mars with mro/marci. Icarus 332, 24–49. http://dx.doi.org/10.1016/j.icarus.2019.05.041.

Wolff, M.J., Fernando, A., Smith, M.D., Forget, F., Millour, E., Atwood, S.A., Jones, A.R., Osterloo, M.M., Shuping, R., Shamsi, M.Al., Jeppesen, C., Fisher, C., 2022. Diurnal variations in the aphelion cloud belt as observed by the Emirates Exploration Imager (EXI). Geophys. Res. Lett. 49, e2022GL100477. http://dx.doi.org/10.1029/2022GL100477.

Wu, Z., Li, T., Dou, X., 2017. What causes seasonal variation of migrating diurnal tide observed by the mars climate sounder? J. Geophys. Res.: Planets 122, 1227–1242. http://dx.doi.org/10.1002/2017JE005277.